

Flow leakage and Kelvin–Helmholtz instability of turbulent flow over porous media

Cite as: Phys. Fluids **34**, 105114 (2022); <https://doi.org/10.1063/5.0111195>

Submitted: 18 July 2022 • Accepted: 09 September 2022 • Accepted Manuscript Online: 12 September 2022 • Published Online: 10 October 2022

 Mohammad Jadidi,  Hanieh Khalili Param,  Alistair Revell, et al.



[View Online](#)



[Export Citation](#)



[CrossMark](#)

ARTICLES YOU MAY BE INTERESTED IN

Thin film evaporation: New insights with nanofluid inclusion and component of the electrostatic interactions

Physics of Fluids **34**, 102005 (2022); <https://doi.org/10.1063/5.0117978>

A study of Novec 649TM fluid jets injected into sub-, trans-, and supercritical thermodynamic conditions using planar laser induced fluorescence and elastic light scattering diagnostics

Physics of Fluids **34**, 102106 (2022); <https://doi.org/10.1063/5.0106473>

Experimental investigation of the flow features around an elliptical Ahmed body

Physics of Fluids **34**, 105119 (2022); <https://doi.org/10.1063/5.0114377>



Physics of Fluids

Special Topic: Paint and Coating Physics

Submit Today!

Flow leakage and Kelvin–Helmholtz instability of turbulent flow over porous media

Cite as: Phys. Fluids **34**, 105114 (2022); doi: [10.1063/5.0111195](https://doi.org/10.1063/5.0111195)

Submitted: 18 July 2022 · Accepted: 9 September 2022 ·

Published Online: 10 October 2022



Mohammad Jadidi,¹ Hanieh Khalili Param,² Alistair Revell,¹ and Yasser Mahmoudi^{1,a}

AFFILIATIONS

¹Department of Mechanical, Aerospace and Civil Engineering (MACE), University of Manchester, Manchester M13 9PL, United Kingdom

²Department of Mechanical, Automotive and Material Engineering (MAME), University of Windsor, Ontario N9B 3P4, Canada

^aAuthor to whom correspondence should be addressed: yasser.mahmoudilarimi@manchester.ac.uk

ABSTRACT

In the present paper, turbulent flow in a composite porous–fluid system, including a permeable surface-mounted bluff body immersed in a turbulent channel flow, is investigated using pore-scale large eddy simulation. The effect of Reynolds number (Re) on the flow leakage from porous to non-porous regions, Kelvin–Helmholtz (K–H) instabilities, as well as coherent structures over the porous–fluid interface are elaborated by comparing cases with three Reynolds numbers ($Re = 3600, 7200$, and $14\,400$). Results show that more than 52% of the fluid entering the porous blocks leaks from the first half of the porous region to the non-porous region through the porous–fluid interface. As the Re number increases from 3600 to $14\,400$, the flow leakage decreases by 24%. Flow visualization shows that the Re number affects the size of counter-rotating vortex pairs (CRVPs) and coherent hairpin structures above the porous block. At the $Re = 3600$, the CRVPs are larger and their centers locate farther away from the porous–fluid interface at $Y/D \sim 0.3$ (D is two times of the distance between the centers of two consecutive pores), while at the highest Re number ($Re = 14\,400$), they are 200% smaller and their centers become closer to the interface at $Y/D \sim 0.1$. Moreover, turbulence statistics show that by reducing the Re number, turbulence production is delayed downstream; at the $Re = 14\,400$, it begins from the leading edge of the porous block ($X/D = 0$), while at the $Re = 3600$, turbulence production is postponed and starts nearly at the middle of the porous block ($X/D = 4.6$). Also, quadrant-hole analysis indicates that increasing the Re number from 3600 to $14\,400$ strengthens sweep events and submerges the legs of coherent hairpin structures into the interface. Finally, the distribution of the pressure gradient for the three Re numbers confirms the occurrence of the K–H instability vortices over the porous–fluid interface. For $Re = 3600$, the K–H instability vortices show a linear growth rate in the vertical and horizontal directions with the slope of 0.136 and 0.05 , respectively. However, by increasing the Re from 3600 to $14\,400$, the growth rate slope in the horizontal direction decreases by nearly 33.8%, while in the vertical direction, it increases by 200%.

Published under an exclusive license by AIP Publishing. <https://doi.org/10.1063/5.0111195>

NOMENCLATURE

A_p	Surface area of solid obstacles, m^2	Q	Second invariant of velocity gradient tensor, $1/\text{s}^2$
b_{ij}	Reynolds stress anisotropy tensor	$Re = UH/\vartheta$	Reynolds number based on inlet bulk velocity and channel height, -
D	Two times the distance between the centers of two consecutive pores, m	$Re_D = UD/\vartheta$	Reynolds number based on inlet bulk velocity and D
D_p	Mean pore element diameter, m	Re_k	Permeability Re number ($Re_k = (U\sqrt{K})/\vartheta$)
h	Porous block height, m	S_{ij}	Strain rate tensor, $1/\text{s}$
H	Channel height, m	\bar{S}_{ij}	Resolved strain rate tensor, $1/\text{s}$
K	Permeability, m^2	T	Time, s
K	Turbulence kinetic energy, m^2/s^2	$T^* = \Delta t/(D/U)$	Non-dimensional time unit, -
P	Pressure, Pa	U	Streamwise velocity component, m/s
P_k	Turbulence production, m^2/s^3	U	Inlet bulk velocity, m/s

u'_i	Velocity fluctuation in i^{th} direction,
$u'_i = \bar{u}_i - \langle \bar{u}_i \rangle$, m/s	
V	Vertical velocity component, m/s
V_p	Volume of solid obstacles, m ³
X	Streamwise direction, m
Y	Vertical direction, m
Z	Lateral direction, m
Δt	Time step, s
Δy	Mean cell size in the vertical direction, m

Symbol

ρ	Density, kg/m ³
Δ	Filter width, m
$\Delta\delta_1$	Vortex size in the streamwise direction, m
$\Delta\delta_2$	Vortex size in the vertical direction, m
ε_t	Total dissipation, m ² /s ³
ζ	Distance of any arbitrary point with respect to a reference point, m
η	Second invariants of b_{ij}
Θ	Molecular kinematic viscosity, m ² /s
$\lambda_1, \lambda_2, \lambda_3$	Eigenvalues of tensor b_{ij}
ξ	Third invariants of b_{ij}
τ_{ij}	Residual (SGS) shear stress, m ² /s ²
ϑ_{SGS}	Sub-grid scale eddy viscosity, m ² /s
Φ	Porosity, -
Ω_{ij}	Rotation rate tensor, 1/s
$\langle \rangle$	Time-averaged value, -

Subscript

In	Inlet
Exp	Experimental
Num	Numerical
Res	Resolved
RMS	Root mean square
SGS	Sub-grid scale
Solid	Solid block

Superscript

- Filtration and also ensemble averaging operator in “Quadrant-Hole analysis” section
- ' Fluctuation

Abbreviation

CFL	Courant–Friedrichs–Lewy number, -
TKE	Turbulent kinetic energy, m ² /s ²

I. INTRODUCTION

Flow over and through the porous media is encountered in several natural phenomena and a wide range of industrial applications. Cooling of electronic devices with metal foam heat sinks,^{1–3} energy storage systems,^{4,5} heat exchangers,^{6,7} noise control in the aerospace industry,^{6,8,9} and flow over vegetation in the canopies in environmental engineering^{10–12} can be a few examples of typical flow over and

through the porous media. Remarkable research has been conducted in literature either experimentally or numerically to explore the flow physics over fluid-saturated porous media. However, the governing physics that characterizes porous wall flows has not been well understood compared to solid wall flow. The significant challenging phenomenon lies in the interaction of the flow with the porous structure at the interface between the porous and non-porous regions. The primary measured data^{13–16} evidenced that the wall permeability affects the turbulent flow near the porous wall differently from the wall roughness, raising the momentum exchange,^{13,14} and there are sharp gradients between the porous and non-porous flows which demonstrate the existence of slip velocity at the interface.¹⁵ The advent of particle image velocimetry (PIV) has enabled qualitative and quantitative insights into flow-visualization data of porous wall flows.^{17–20} Suga *et al.*²¹ conducted experiments on a turbulent channel flow with a porous bottom wall to determine the effect of wall permeability and Reynolds number on the turbulent flow regime near the porous wall. The results proved that compared to solid walls, the transition of flow from laminar to turbulent occurs at lower Re numbers for the porous cases.²¹ Manes *et al.*²² performed experiments to answer the challenging question of how the flow interacts with the porous structure at the interface between the surface and subsurface flows. Similar to the findings by Suga *et al.*,²¹ they confirmed that friction forces are significantly affected by wall permeability.²² Kim *et al.*¹⁸ investigated the effect of critical parameters, including wall permeability and surface topography, on the flow interactions between the surface and subsurface flows.¹⁸ The results of instantaneous velocity fluctuations near the porous–fluid interface revealed the existence of a strong negative correlation between the surface and subsurface flows. In recent years, numerical simulations have been performed increasingly to explore flow dynamics accurately in subsurface and surface flow regions due to the difficulties involved in measuring the local properties of flow through and above porous blocks in experiments.^{23–27} Chu *et al.*²⁵ performed direct numerical simulations (DNS) to explore the flow interaction between the clear fluid region and inside the pore scale. For this purpose, two Re numbers, 3000 and 6000, and two porosities ($\Phi = 0.5$ and 0.8) were considered. The results proved that the porosity significantly impacts the fluid motion near the interface and, consequently, turbulence transportation. The turbulent kinetic energy (TKE) budgets demonstrated that pressure transportation and turbulent diffusion play the role of energy source and sink, which provide the possibility of turbulence transportation from the clear fluid into the porous region.²⁵

Despite several studies in the literature on turbulent flows over fluid–porous systems, there is still a paucity of fundamental knowledge about the evolution of the Kelvin–Helmholtz (K–H) instability over the fluid–porous interface. Only a few studies, to the best of the authors' knowledge, have carried out specifically detailed discussions on the K–H instabilities' formation over fluid-saturated porous media.^{20,23,28–30} In the DNS study of Breugem *et al.*,²³ the volume-averaged Navier–Stokes (VANS) equations were engaged to describe the flow dynamics within the porous structures consisting of various wall permeabilities. Increasing the wall permeability yields in the formation of the comparatively larger vortical structures above the pore scales associated with the Kelvin–Helmholtz (K–H) instabilities. These vortical structures are responsible for the TKE transport and momentum exchange between the surface and subsurface flows. Raise in

Reynolds shear stress and, consequently, skin friction is attributed to this interaction.²³ In the case study of flow over densely submerged vegetation canopy channel, Nepf and Ghisalberti²⁸ noted the crucial contribution of K-H instabilities to generating vortical structures in the shear layer. These structures strongly manipulate the vertical transfer of momentum and mass, impacting the mean velocities and TKE transport. Through the experimental study of the turbulent channel flow with a porous bottom wall, Suga *et al.*²⁰ investigated the effect of the wall permeability on the turbulent vortex development near the fluid-porous interface. A conceptual scenario was substantiated to describe the generation and progression mechanisms of the vortex structures near the porous wall at the relatively moderate permeability Re number (Re_k). This scenario also explains that by moving downstream the hairpin-like vortical structures generated by the interaction of the main flow with the blown low-speed fluid lump from pore holes would lose their legs. Recently, Suga *et al.*³⁰ have performed PIV measurements to evaluate the fully developed turbulent channel flow (at two Re numbers $\cong 3500$ and 7500) composed of square-sectioned pore-scales at the bottom wall. It was shown that at high permeability Re numbers, the wavelength of spanwise rollers at the symmetry-plane, established by K-H instabilities, is similar to those at the porous structure. However, at relatively low-permeability Re numbers due to the sidewall effects, the wavelengths would be shortened compared to those of the pore-scale region. Additionally, in a composite porous-fluid system, recent experimental studies have demonstrated that, for specific blockage ratios and pore densities, the fluid in the porous region is pushed upward into the non-porous region at the porous-fluid interface before reaching the porous block end (flow leakage).^{31,32} Recently, the flow exchange and heat transfer between porous and non-porous regions in a composite porous-fluid system with $Re = 3600$ are studied numerically by Jadidi *et al.*,³³ using pore-scale large-eddy simulation (LES). The results of two porous structures, consisting of rectangular rods and packed beds of spheres, have been compared with those of solid blocks.

The flow leakage at the porous-fluid interface makes the physics of fluid and heat transfer very complex in composite porous-fluid

systems. According to the literature review, the physics underlying the flow leakage from the porous region to the non-porous region and the evolution of the K-H instability vortices over the porous-fluid interface has not been well understood yet. It should be noted that previous pore-scale studies in the literature have mainly focused on the fully developed channel flow with periodic inlet and outlet boundary conditions, where the bottom wall is fully covered by a porous medium.^{17,18,20,25} Thus, for those studies, the wake generation behind the porous block, separation over the porous interface, and stagnation on the windward face of the porous block, as well as their interaction with the interface flow leakage, have not been discussed in detail. In addition, to the best of the authors' knowledge, there is a substantial paucity of knowledge in the literature on the flow over composite porous-fluid systems consisting of a porous bluff body (see Fig. 1). This is because the majority of studies have concentrated on the partially filled channel flow where the bottom wall is fully covered with the porous medium. The present paper focuses on turbulent flow physics over a porous medium using pore-scale large-eddy simulation deploying quadrant-hole analysis, probability density function (PDF) of velocity fluctuations, and turbulence anisotropy analysis. The emphasis is placed on understanding the effect of the Re number in the range of $Re = (3600–14\,400)$ on the flow leakage and evolution of K-H instabilities over the porous-fluid interface. The key reason for selecting this range is that the onset and evolution of K-H instabilities within different flow structures can be observed in this range.

II. COMPUTATIONAL METHODOLOGY

B. Geometry and computational domain

Figure 1 displays a schematic of the computational geometry representing a turbulent internal flow in a channel partially filled with a permeable porous bluff body. The ratio of the porous region height (h) to that of the channel (blockage ratio) is $h/H = 0.5$. The porous blocks are composed of rectangular cross section ($0.52D \times 0.52D$) ligaments with a thickness of $0.26D$, representing a porosity of $\Phi = 48\%$. All dimensions in this study are normalized by $D = 6\text{ mm}$

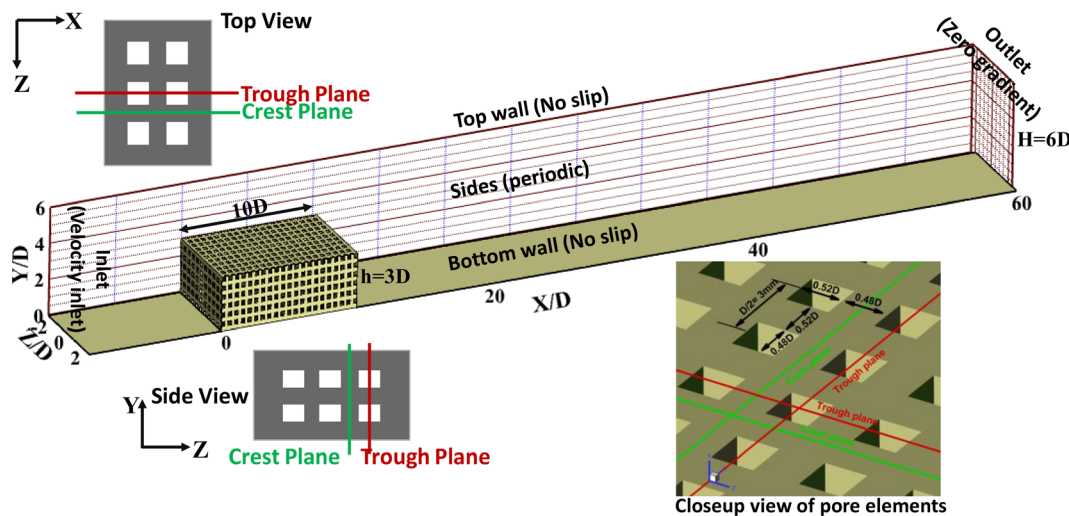


FIG. 1. Computational domain composed of a porous block with a porosity of $\Phi = 48\%$, boundary conditions applied in the current LES study, and definition of two spanwise and streamwise planes for presenting the LES results; the red line lies over the trough plane, and green line lies over the crest plane.

TABLE I. Boundary conditions implemented at different boundaries.

Inlet boundary	Uniform inlet velocity boundary: $U = 1, 2, \text{ and } 4$ for $Re = 3600, 7200, \text{ and } 14\,400$.
Outlet boundary	Zero static pressure and zero gradient condition for all the other flow variables.
Side boundaries	Periodic boundary condition.
Top and Bottom walls	No slip.

parameter, where D is two times of the distance between the centers of two consecutive pore elements. The computational domain extends $70D \times 6D \times 5D$ in the streamwise, vertical and lateral directions, respectively. Three cases are examined, namely, cases 1, 2, and 3. Correspondingly, based on the inlet bulk velocity (U) and channel height (H), the flow Re numbers are 3600, 7200, and 14 400 for cases 1, 2, and 3. The implemented boundary conditions are presented in [Fig. 1](#) and [Table I](#). Different planes at spanwise and streamwise locations, namely, “trough plane” and “crest plane,” are defined (as shown in [Fig. 1](#)) to illustrate the present LES results. Due to the difference in permeability at “trough” and “crest” locations, porous block experiences pronounced different flow dynamics over these planes. For instance, the fluid–solid interface at the crest plane is locally impermeable, preventing any flow exchange between surface and subsurface. On the contrary, the trough plane possesses a fully open (permeable) interface, allowing fluid transfer between two distinct regions. Hence, the LES results at these two planes would exhibit various flow heterogeneities induced by surface topography and different wall permeabilities. Instead of a separate calculation for the permeability (K) of the porous block composed of the rectangular cross section, it was estimated by the Carman–Kozeny model^{23,34}

$$K = \frac{\Phi^3}{180(1 - \Phi)^2 D_p^2}. \quad (1)$$

Here, $D_p = 6V_p/A_p$ is the mean particle diameter for which V_p and A_p represent the volume and surface area of solid obstacles, respectively. By this equation, $K = 2.85 \times 10^{-8} \text{ m}^2$ for the current porous block. Accordingly, the corresponding permeability Reynolds numbers ($Re_K = U\sqrt{K}/\vartheta$) are 16.88, 33.76, and 67.52 for three investigated Re numbers (cases 1–3).

B. Governing equations

The three-dimensional (3D), incompressible and unsteady continuity and momentum (Navier–Stokes) equations are subjected to a top-hat filter (equal to grid size) in the present LES study as follows:^{35,36}

$$\frac{\partial \bar{u}_i}{\partial X_i} = 0, \quad (2)$$

$$\frac{\partial \bar{u}_i}{\partial t} + \frac{\partial}{\partial X_j} (\bar{u}_i \bar{u}_j) = -\frac{1}{\rho} \frac{\partial \bar{p}}{\partial X_i} + \frac{\partial}{\partial X_j} \left((\vartheta) \frac{\partial \bar{u}_i}{\partial X_j} \right) - \frac{\partial \tau_{ij}}{\partial X_j}, \quad (3)$$

where (\dots) and ϑ refer to the filtration operation and molecular viscosity, respectively. The contribution of instantaneous smaller scales

(sub-grid scales) that are removed through filtering is taken into account by the advent of unclosed residual shear stress (τ_{ij}), signifying the influence of the sub-grid scales (SGS) on the resolved ones. The SGS turbulent stress tensor (τ_{ij}) is estimated by a similar approach to the Boussinesq hypothesis.³⁶

$$\tau_{ij} = \bar{u}_i \bar{u}_j - \bar{u}_i \bar{u}_j, \quad (4)$$

$$\tau_{ij} - \frac{1}{3} \tau_{kk} \delta_{ij} = -2\vartheta_{SGS} \bar{S}_{ij} = -2C_\tau \Delta k_{SGS}^{1/2} \bar{S}_{ij}. \quad (5)$$

Here, ϑ_{SGS} , k_{SGS} , and \bar{S}_{ij} are the SGS turbulent eddy viscosity, SGS turbulence kinetic energy, and resolved strain rate tensor, respectively. In the present study, localized dynamic k_{SGS} -equation model (LDKM)³⁷ was utilized to estimate ϑ_{SGS} . In this model, a transport equation [Eq. (7)] is engaged to calculate the k_{SGS}

$$k_{SGS} = \bar{u}_k \bar{u}_k - \bar{u}_k \bar{u}_k, \quad (6)$$

$$\frac{\partial k_{SGS}}{\partial t} + \frac{\partial (u_i k_{SGS})}{\partial X_i} = \frac{\partial}{\partial X_i} \left[\frac{\vartheta_{SGS} \partial k_{SGS}}{\sigma_k} \right] - C_\epsilon \frac{k_{SGS}^{3/2}}{\Delta}, \quad (7)$$

where $\sigma_k=1$ and Δ is the filter width. Also, C_ϵ and C_τ are the model constants which are determined dynamically.³⁷

C. Numerical procedure

The finite volume method (FVM) was utilized to discretize the filtered governing equations. The velocity and pressure fields are coupled via the PIMPLE algorithm within an open-source, object-oriented C^+ programming CFD package (OpenFOAM V9³⁸). The second-order central differencing scheme was employed for spatial discretization, and the second-order implicit method (backward scheme) was used for time derivatives.³⁸ The physical time step was chosen in such a way that keeps the Courant–Friedrich–Lewy (CFL) number at or below unity so that the flow features’ evolution can be captured accurately. This yielded a constant non-dimensional time step of $\Delta t/(D/U) = 8.3 \times 10^{-4}$ which satisfies the CFL number condition for most of the refined cells. The data sampling process was launched when the initial transient conditions were washed out and a statistically semi-steady state-operating condition was attained. The time-dependent variables are averaged at least over a period of non-dimensional time $T^* = \Delta t/(D/U) = 490$. The details of numerical procedure are summarized in [Table II](#).

The grid resolution was assessed by three different criteria, including the ratio of the SGS eddy viscosity to molecular viscosity,^{39,40} the ratio of the resolved kinetic energy (k_{res}) to total turbulent kinetic energy (TKE),⁴¹ and the two-point correlations method.⁴² Two-point correlations can be employed as the indicators of the spatial scales to determine by how many cells the largest scales are resolved.^{43,44} The

TABLE II. Details of the numerical procedure.

Pressure–velocity coupling algorithm	PIMPLE algorithm (combination of SIMPLE and PISO algorithm)
Time discretization	Second-order implicit method (backward scheme)
Convection term discretization	Second-order central differencing scheme
Time step size, Δt	$\Delta t/(D/U) = 1.0 \times 10^{-4}$
Sampling time	$T^* = \Delta t/(D/U) = 490$

TABLE III. Ratio of the integral length scale to the grid spacing in the vertical direction.

Cases	$\lambda_{uu-Y}/\tilde{\Delta Y}$	$\lambda_{vv-Y}/\tilde{\Delta Y}$
Case 1 ($Re = 3600$)	7.81	6.38
Case 2 ($Re = 3600$)	6.64	6.12
Case 3 ($Re = 14400$)	5.34	5.14

size of the largest eddies (energy-containing eddies), called integral length scales, can be estimated by the integral of the spatial correlations.^{43,45} The tow-point correlation of velocity field (u) in a direction like the Y-direction can be defined as

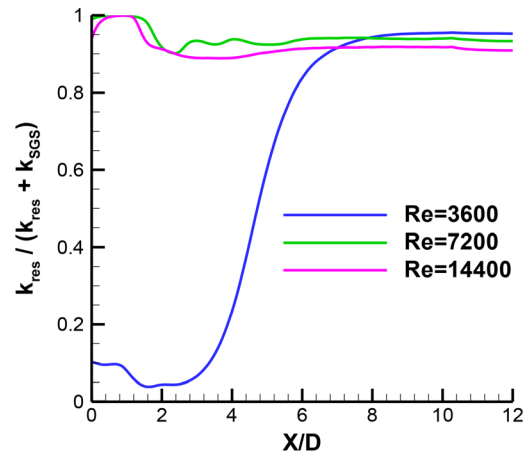
$$R_{uu-Y}(\zeta) = \frac{\langle u'(Y_{ref}).u'(Y_{ref} + \zeta) \rangle}{\sqrt{\langle u'(Y_{ref})^2 \rangle \langle u'(Y_{ref} + \zeta)^2 \rangle}}, \quad (8)$$

$$\lambda_{uu-Y} = \int_0^\infty R_{uu-Y}(\zeta) d\zeta. \quad (9)$$

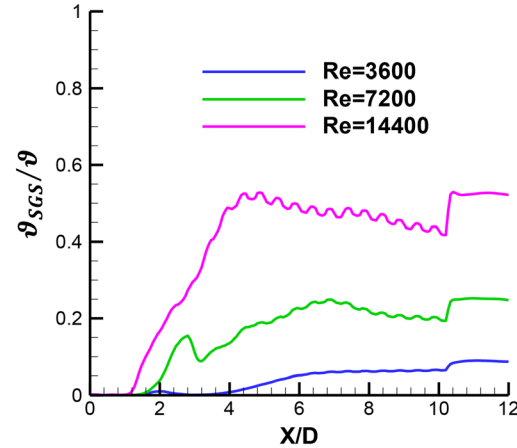
Here, $\langle \dots \rangle$ denotes the time-averaging operation. Also, u' indicates the velocity fluctuations ($u' = \bar{u} - \langle \bar{u} \rangle$), Y_{ref} refers to the Y-position of the reference point, ζ is the distance of any arbitrary point in the

Y-direction with respect to a reference point, and λ_{uu-Y} is the integral length scale. Ratios of the integral length scale to mean grid spacing ($\lambda_{uu-Y}/\Delta y$) can be an appropriate metric for grid resolution assessment since it illustrates the average number of the cells in the resolved largest scales. Since the mesh is non-uniform in the vertical direction, the mean grid spacing (Δy) in the vertical direction is considered for calculating this ratio. Table III explains the ratio of the integral length scale (calculated from streamwise and vertical velocity components) to the average cell size in the vertical direction (Δy) at the center plane ($Z/D = 0$) along the line $X/D = 12$. As shown in Table III, at least five grids are included in the vertical integral length scale, which means the sufficient accuracy of the grid.^{42,43}

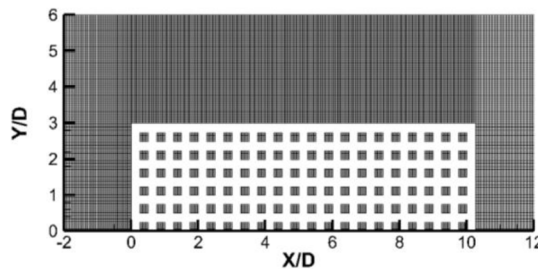
Moreover, the grid resolutions satisfy other grid assessment techniques, such as the ratio of SGS turbulent viscosity to the physical one, $\vartheta_{SGS}/\vartheta$,⁴⁶ and the ratio of the resolved to total TKE, $k_{res}/(k_{SGS} + k_{res})$,⁴¹ as depicted in Figs. 2(a) and 2(b), for a horizontal line $Y/D = 3.85$. It should be mentioned that at $Re = 3600$, the ratio of the resolved to total TKE before $X/D \cong 6$ is less than 80% which does not mean the mesh possesses a low quality and grid resolution does not pass this criterion. In fact, at $Re = 3600$ before $X/D \cong 6$, the flow is laminar, which will be discussed in Sec. III E (Turbulent production) comprehensively. Thus, in this region, the ratio of the resolved to total TKE criterion is not applicable to assess the grid resolution.



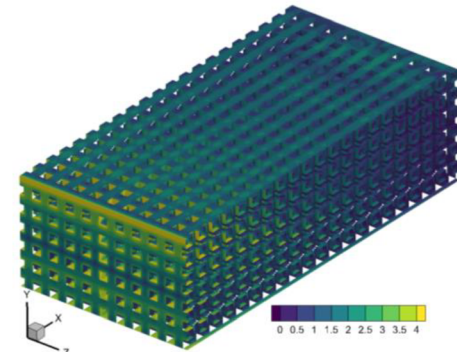
a) Ratio of the resolved to total TKE along the porous block at $Y/D=3.85$



b) Ratio of SGS to physical viscosity along the porous block at $Y/D=3.85$



c) Grid resolution distribution on the crest plane



d) Contour of y_p^+ over the porous block

FIG. 2. Grid resolution assessment; (a) $k_{res}/(k_{SGS} + k_{res})$, (b) $\vartheta_{SGS}/\vartheta$, (c) grid distribution, and (d) contour of y_p^+ .

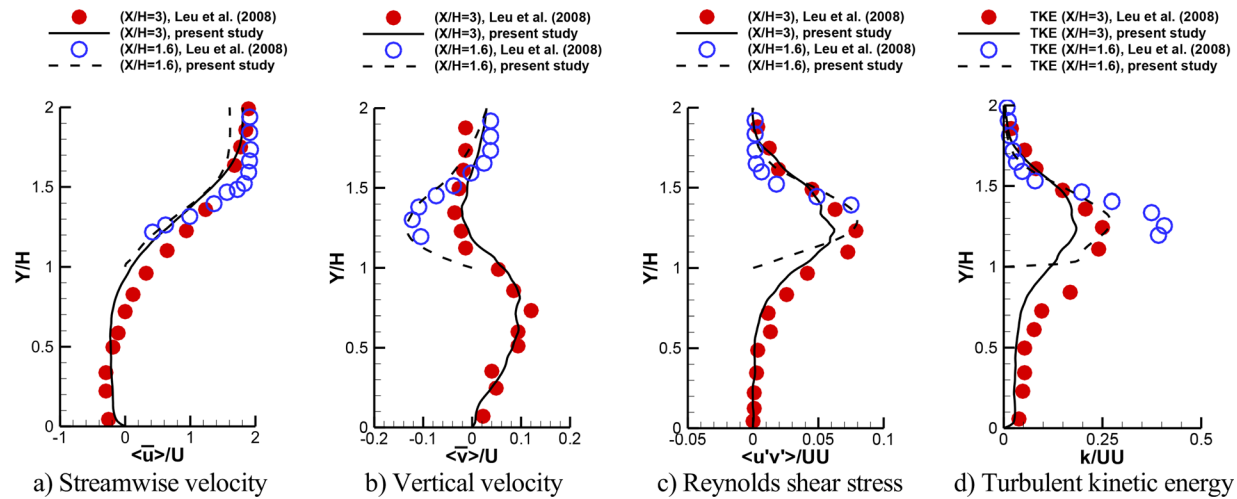


FIG. 3. Vertical variations of non-dimensional time-averaged streamwise velocity, vertical velocity, Reynolds shear stress, and turbulent kinetic energy (TKE) compared with the experimental data of Leu *et al.*⁴⁷ at two locations: $X/D = 1.6$ and $X/D = 3.0$; (a) streamwise velocity, (b) vertical velocity, (c) Reynolds shear stress, and (d) turbulent kinetic energy.

D. Validation

Before presenting the LES results of the composite porous–fluid system, the code has been verified by the LES calculations of another test case generated based on the experimental setup of Leu *et al.*⁴⁷ In their study, measured data of velocity components and turbulence statistics were provided within a circulating flume composed of a porous bottom wall. The porous block consisted of glass beads with diameters of $D = 0.015$ m arranged in a non-staggered pattern representing a porosity of 47.5%. The block had a length (L), width (W), and height (H) of 0.15, 0.3, and 0.075 m, respectively, and was positioned at $38.9H$ downstream of the inlet of the test bed. Owing to the long distance between the block and inlet of the test section and, consequently, heavy computational costs of the LES study, this distance was reduced to $4H$. Instead, the Divergence-Free Synthetic Eddy Method (DFSEM)⁴⁸ was superimposed on the RANS results of a full domain for turbulence inflow generation at the inlet cross section of the LES computational geometry. The present LES results are compared with the measured data of Leu *et al.*⁴⁷ for various parameters, including streamwise and vertical velocities, Reynolds shear stress, and turbulent kinetic energy [$k = 0.5(\langle u'^2 \rangle + \langle v'^2 \rangle + \langle w'^2 \rangle)$] at two locations: above the porous block, $X/D = 1.6$ and in the wake region, $X/D = 3.0$. As shown in Fig. 3, the LES results are in reasonable agreement with the measured data. To validate the implemented code in the present study, the pressure drops of another LES study by the current authors are compared against the reference data.^{49–51} The pressure drops of the fluid flow inside a porous channel, which is filled with spheres of $D = 6.0$ mm, vs Reynolds number (Re_D , based on the spheres diameter and inlet velocity), are shown in Fig. 4. In general, the predicted pressure drops are in good agreement with the available reference data in the literature.^{49–51}

III. DISCUSSION OF RESULTS

A. Flow leakage

Time-averaged streamwise and vertical velocity contours on the crest and trough planes are depicted in Figs. 5 and 6 for the three Re

numbers. The velocity components are made non-dimensional with their corresponding inlet bulk velocity (U). In Figs. 5(a), 5(c), and 5(e), on the crest plane, three distinct turbulent separation bubbles (hereafter denoted by TSB) can be recognized; TSB1: an upstream separation bubble in front of the windward face of the porous block, TSB2: a primary recirculation region on the porous–fluid interface, TSB3: a wake region behind the leeward face of the porous block. Mean streamwise velocity contours at the trough planes [Figs. 5(b), 5(d), and 5(f)] demonstrate that the flow leakage from the porous block to the non-porous region prevents the generation of a distinct TSB2, especially for the lowest Re number ($Re = 3600$), due to possessing higher flow exchange (which will be detailed in Fig. 8 and Table IV). Thus, for

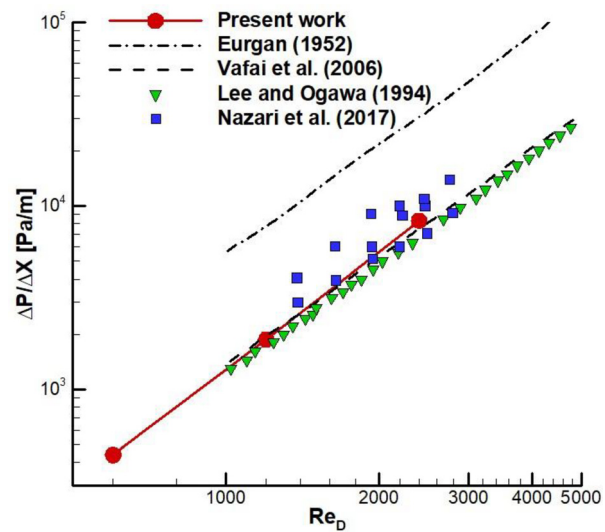


FIG. 4. Comparison of pressure drops in the packed bed with available Refs. 49, 51, and 50.

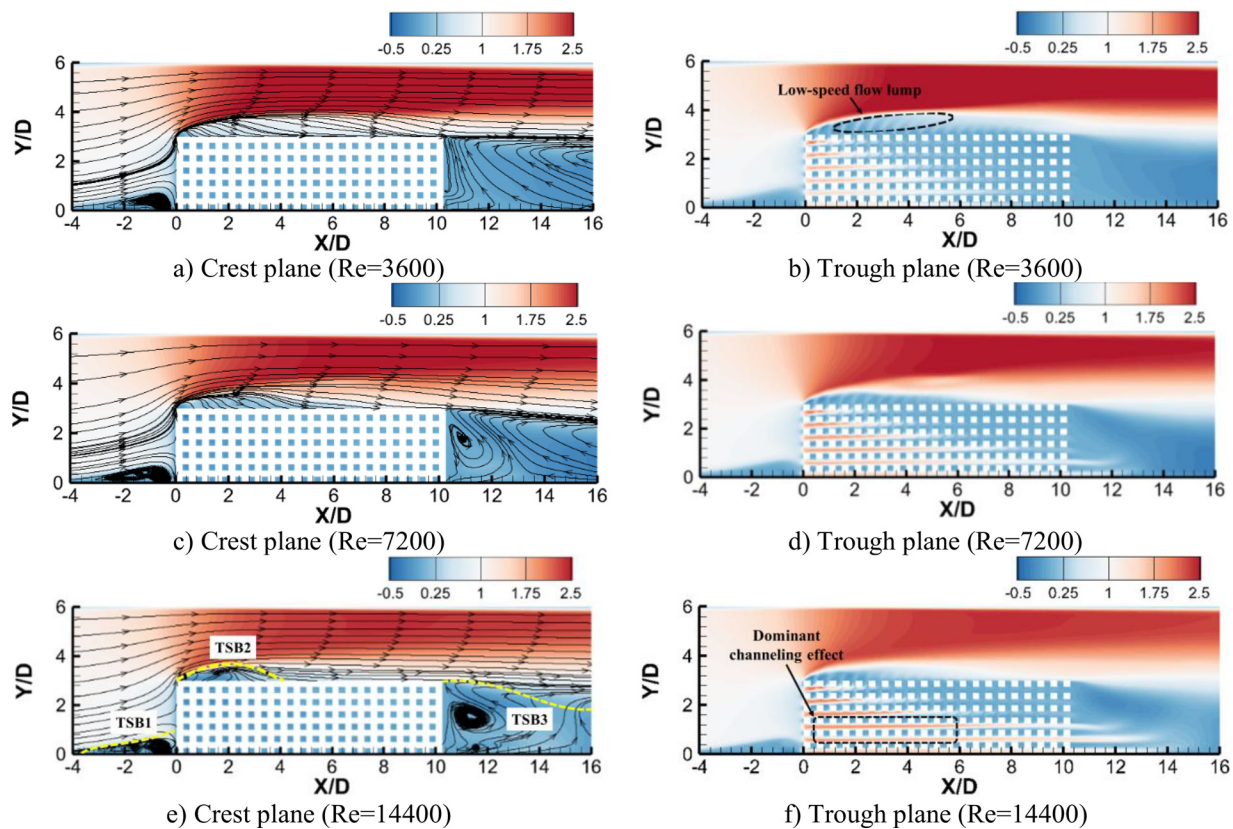


FIG. 5. Contours of non-dimensional time-averaged streamwise velocity ($\langle \bar{u} \rangle / U$) for three cases with different Re numbers at crest and trough planes; (a) and (b) $Re = 3600$, (c) and (d) $Re = 7200$, and (e) and (f) $Re = 14\,400$.

$Re = 3600$, compared to $Re = 14\,400$, the low-speed flow lump [see Fig. 5(b)] above the interface (note: low-speed flow lump indicates a region that has lower velocity compared to its surrounding) tends to stretch toward the trailing edge of the porous block instead of reattaching to the interface (i.e., destruction of TSB2). The distribution of wall shear stress on the porous–fluid interface (not shown here) demonstrates that the size of the TSB2 is shrunk by increasing the Re number. For instance, at $Re = 14\,400$, the length of TSB2 is $2.7D$, while for $Re = 3600$, it covers the whole length of the porous–fluid interface [see Figs. 5(a) and 5(e)]. Overall, two observations should be noted here: (1) as the Re number rises, the streamwise velocity increases at the deeper layers of the porous block [see Figs. 5(b), 5(d), and 5(f)]. Thereby, the channeling effect dominates the flow along trough planes for the higher Re number. This consequently produces streamwise-oriented high-momentum paths in the horizontal direction, which shrinks TSB1 at trough planes for higher Re numbers; (2) as can be seen in Figs. 6(b), 6(d), and 6(f), by decreasing the Re numbers, the flow leakage increases and prevents the generation of TSB2, even though the oncoming flow is separated near the leading edge. In other words, at lower Re numbers, the streamlines demonstrate a continuous upward flow pattern above the interface without any reattachment [see Fig. 5(b)]. Finally, it is observed that the Re number variations do

not have a noticeable impact on the size of the TSB1 generated at the crest planes.

On the crest plane in Fig. 6(a), a strong reverse flow (negative vertical velocity) is apparent just above the interface at $Y/D = 3$. For more illustration, streamlines are displayed in this region in Figs. 7(a) and 7(c) for $Re = 3600$. It can be seen that this flow behavior is related to downward flow motion over the interface on the crest plane and the flow reattachment after the separation on the leading edge of the porous block. Figures 7(b) and 7(d) show that at the trailing edge, some portion of the flow that leaves the porous block to the wake region [forward flow in Fig. 7(d)], reenter to the porous region at a higher height [backward flow in Fig. 7(d)] and then leave the porous region near the interface.

Figure 8 displays the horizontal distribution of the time-averaged non-dimensional vertical velocities on the interface for three Re numbers. The vertical velocity lessens by moving downstream along the interface for each case, meaning that the flow leakage decreases from the leading edge toward the downstream. Also, as illustrated in Fig. 6, the flow leakage reduces as the number Re rises, which is quantified clearly in Fig. 8. A comparison of vertical velocities at different streamwise locations (X/D) implies that a lower Re number possesses a higher vertical velocity and, consequently, a higher flow leakage.

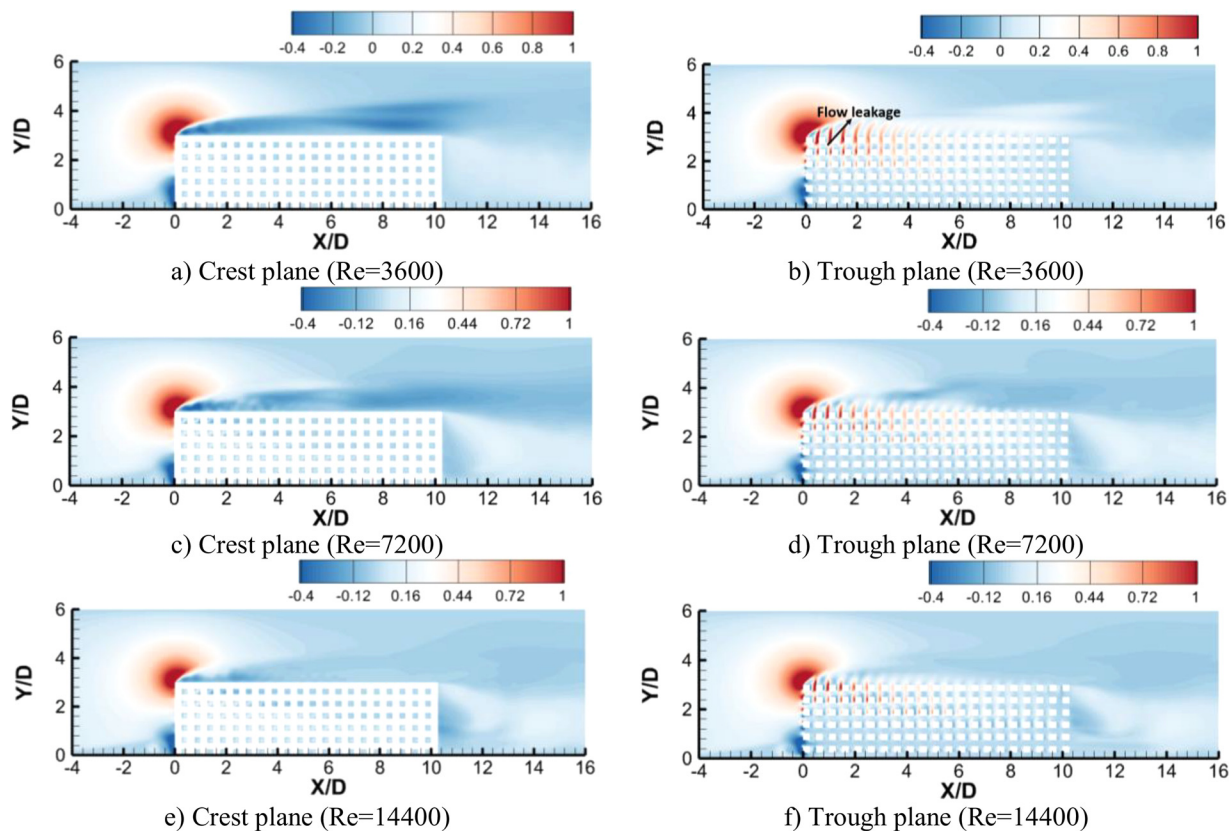


FIG. 6. Contours of non-dimensional time-averaged vertical velocity ($\langle \bar{v} \rangle / U$) for three cases with different Re numbers at crest and trough planes; (a) and (b) $Re = 3600$, (c) and (d) $Re = 7200$, and (e) and (f) $Re = 14400$.

To accurately compare the flow leakage for three Re numbers, Table IV presents the absolute and relative flow rates that drip from the porous block into the non-porous region up to streamwise locations $X/D = 2.5, 5.0$, and 7.5 . A parameter, $Q_{in} = \int_0^{3D} \int_{-2.5D}^{2.5D} \langle \bar{u}(Y, Z) \rangle dZ dY$, is introduced to illustrate the time-averaged flow rate that enters the porous block from the windward face. Additionally, $Q_{IX} = \int_0^X \int_{-2.5D}^{2.5D} \langle \bar{v}(X, Z) \rangle dZ dX$ is the time-averaged flow rate that leaks from the X-percentage of the interface surface. Table IV indicates that the higher the Re number, the larger the flow rate entering the porous block (Q_{in}). In addition, more than 60% of the flow entering the porous blocks exits from the porous interface before $X/D = 7.5$ for three Re

numbers; this even intensifies when the Re number decreases (84% for $Re = 3600$). Finally, relative flow rates (Q_{IX}/Q_{in}) at each streamwise section in Table IV support the discussions in Figs. 6 and 8, demonstrating that increasing the Re number reduces the flow leakage (Q_{IX}).

B. Counter-rotating vortex pairs (CRVPs)

Figure 9 displays the side-view contours of time-averaged streamwise and vertical velocities for three Re numbers at trough planes, $X/D = 2$. Streamlines at these planes indicate the formation of counter-rotating vortex pair (CRVP) flow structures inside the porous block and above the interface. The streamlines exhibit the momentum exchange from the porous block to the non-porous region, highlighting how the CRVPs originate from the deeper layers of the porous block and move upward in the vertical direction toward the interface. Inside the porous block, the size of the CRVPs is restricted to the pore scales, whereas they expand freely above the interface. Figure 9 also illustrates the influence of the Re number on CRVP characteristics. Smaller CRVPs with contracted and closer centers to the interface are associated with the higher Re [Figs. 9(e) and 9(f)]. In comparison, larger CRVPs with stretched and farther centers from the interface are associated with the lower Re [Figs. 9(a) and 9(b)]. This observation is attributed to the difference in momentum exchange for various Re numbers. As seen from vertical velocities in Figs. 9(b), 9(d), and 9(f)

TABLE IV. Relative values of flow rate that leaks from the porous blocks.

X-position along the interface	$Re = 3600$	$Re = 7200$	$re = 14400$
$Q_{in} \times 10^4$	1.54	3.51	7.42
$Q_{IX}/Q_{in} \times 100$	$X = 2.5 D$	44	36
$Q_{IX}/Q_{in} \times 100$	$X = 5.0 D$	68	59
$Q_{IX}/Q_{in} \times 100$	$X = 7.5 D$	84	72
$Q_{IX}/Q_{in} \times 100$	$X = 10 D$	92	78

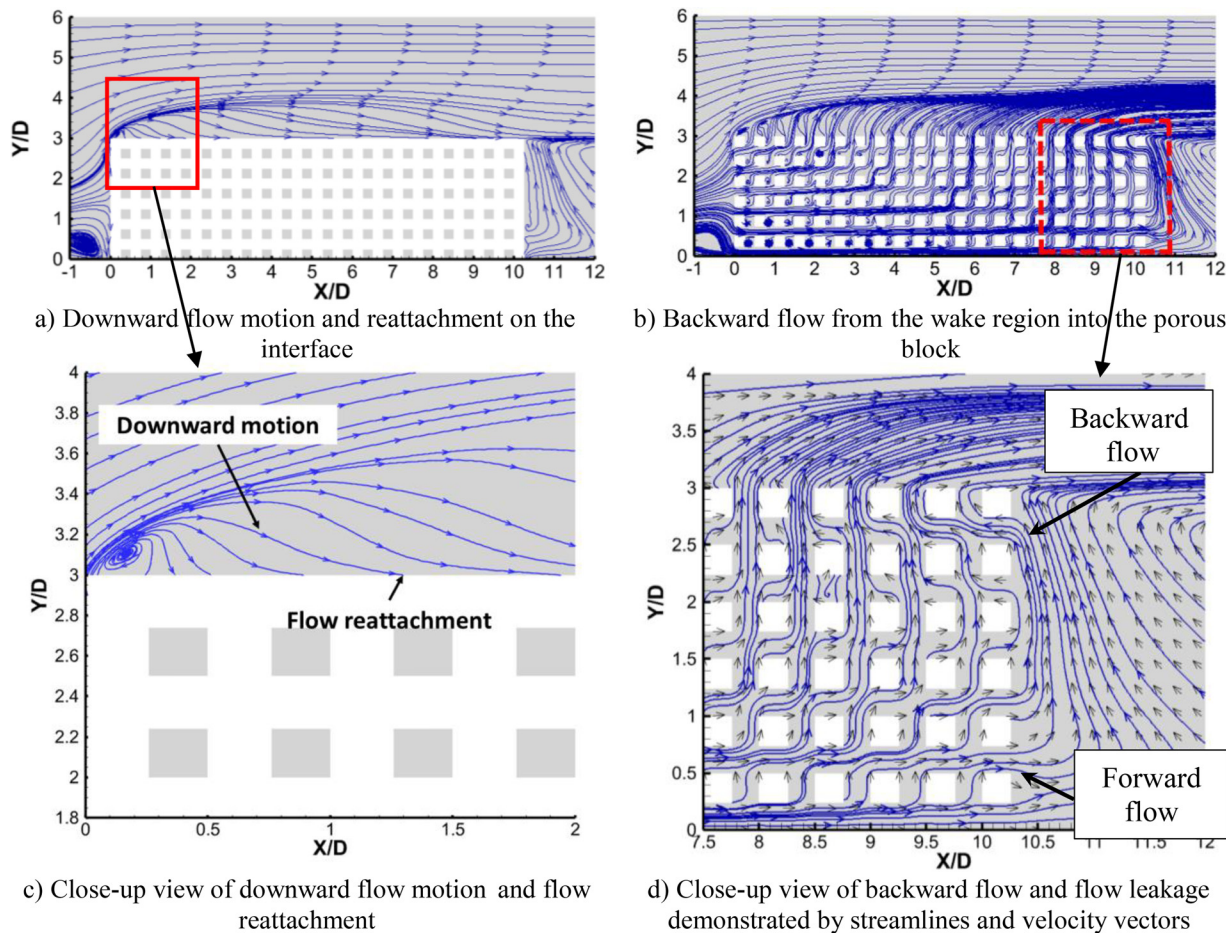


FIG. 7. Flow streamlines at crest and trough planes for $Re = 3600$; (a) downward flow motion and reattachment on the interface, (b) backward flow from the wake region into the porous block, (c) close-up view of the downward flow motion, and (d) close-up view of the backward flow and flow leakage demonstrated by streamlines and velocity vectors

and discussed in Figs. 6 and 8, the flow exchange from the porous to non-porous regions enhances as the Re number decreases. Accordingly, the momentum difference between the upward flow (flow leakage), marked as A, and the low-speed flow lump above the interface, marked as B in Fig. 9(b), enlarges as the Re number decreases, resulting in larger and stretched CRVPs. Finally, the streamwise velocities for three Re numbers in Figs. 9(a), 9(c), and 9(e) witness

the channeling effect described before in Fig. 5. Moving toward the deeper layers of the porous block ($1.5 < Y/D < 2.5$) enhances the streamwise velocity and correspondingly amplifies the channeling effect. This would be more pronounced for higher Re numbers [Fig. 9(e)], underlining higher streamwise velocities in deeper layers and a more powerful channeling effect.

C. Flow structures (hairpins coherent structures)

The hairpin vortex is a fundamental coherent structure in turbulent boundary layers.^{52,53} Adrian *et al.*⁵³ emphasized that the momentum and energy transfer in wall turbulence are associated with the existence of large-scale coherent motions, called hairpin vortex packets and quasi-streamwise vortices, called “one-leg hairpin.” The hairpin packets are composed of a series of hairpin-like vortices that convect coherently. Hairpin vortex packets have been investigated in flows over permeable walls as well.^{20,54,55} Three major components make up a typical hairpin vortex: (1) a vortex head which is a Ω -shaped ring-like vortex and consists of dominant spanwise vorticity, sitting at the farthest distance from the wall; (2) a pair of counter-rotating quasi-

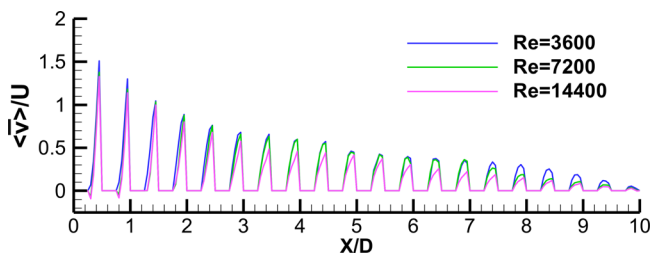


FIG. 8. Horizontal distributions of time-averaged non-dimensional vertical velocity on the interface region for three cases with different Re numbers.

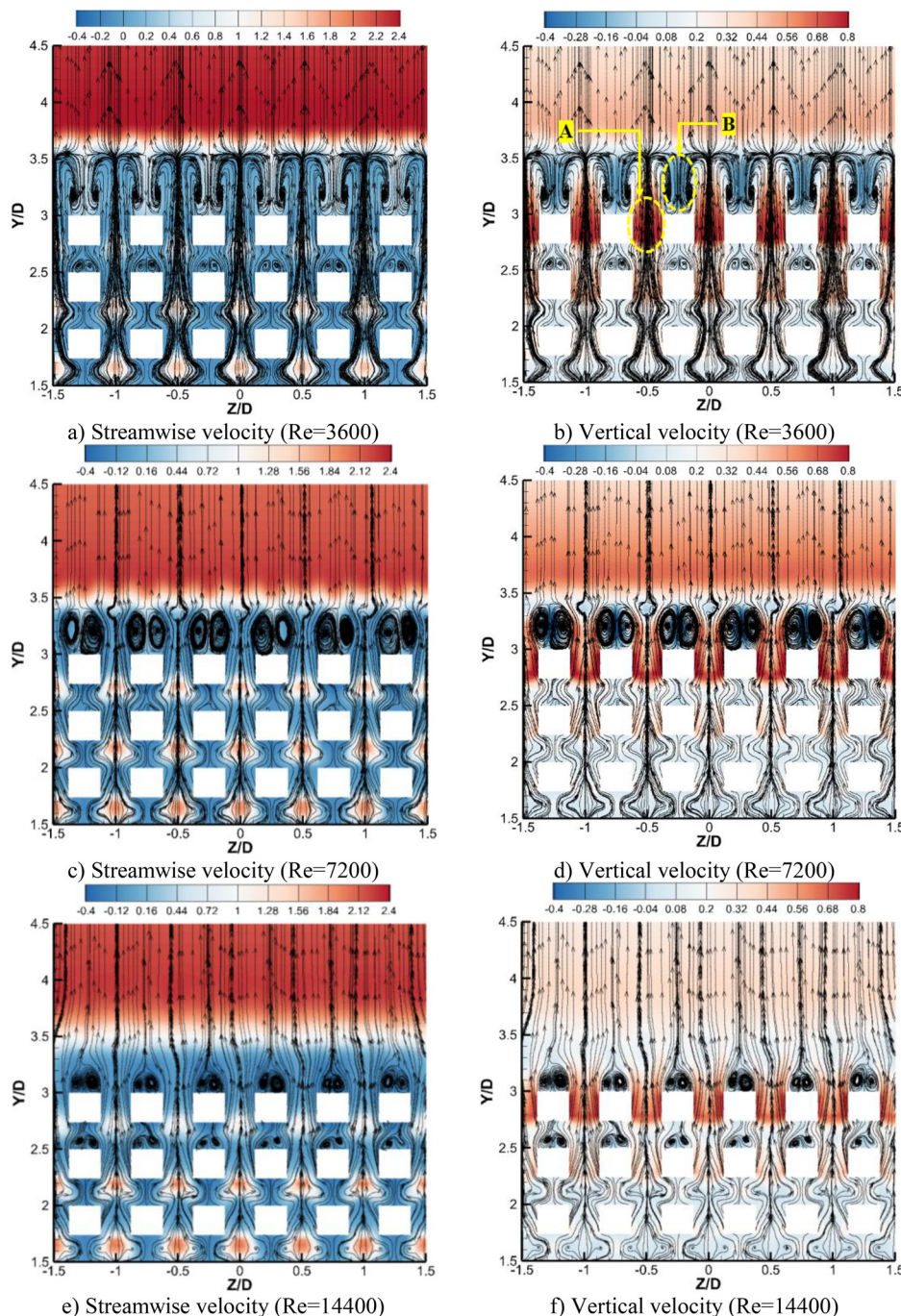


FIG. 9. Side-view contours of time-averaged streamwise and vertical velocity components and streamlines on trough planes ($X/D = 2$); (a) and (b) $Re = 3600$, (c) and (d) $Re = 7200$, and (e) and (f) $Re = 14\,400$.

streamwise vortices adjacent to but not attached to the wall, called as “hairpin legs;” (3) necks connecting the hairpin head and legs together. Suga *et al.*²⁰ examined the vortex structures over permeable walls, and from the quadrant analysis, they concluded that very close to the interface the sweep event becomes more overriding, while in the buffer layer, the ejection event overtakes it.

Figure 10 displays the effect of the Re number on the formation and evolution of the 3D hairpin structures over the porous block. The hairpin vortices are identified by instantaneous iso-surface of second-invariant of velocity gradient tensor, $Q = 0.5 \times (\Omega^2 - S^2)$ and colored by instantaneous streamwise velocity. As a result of the main flow collision with the low-speed flow lump over the interface, at

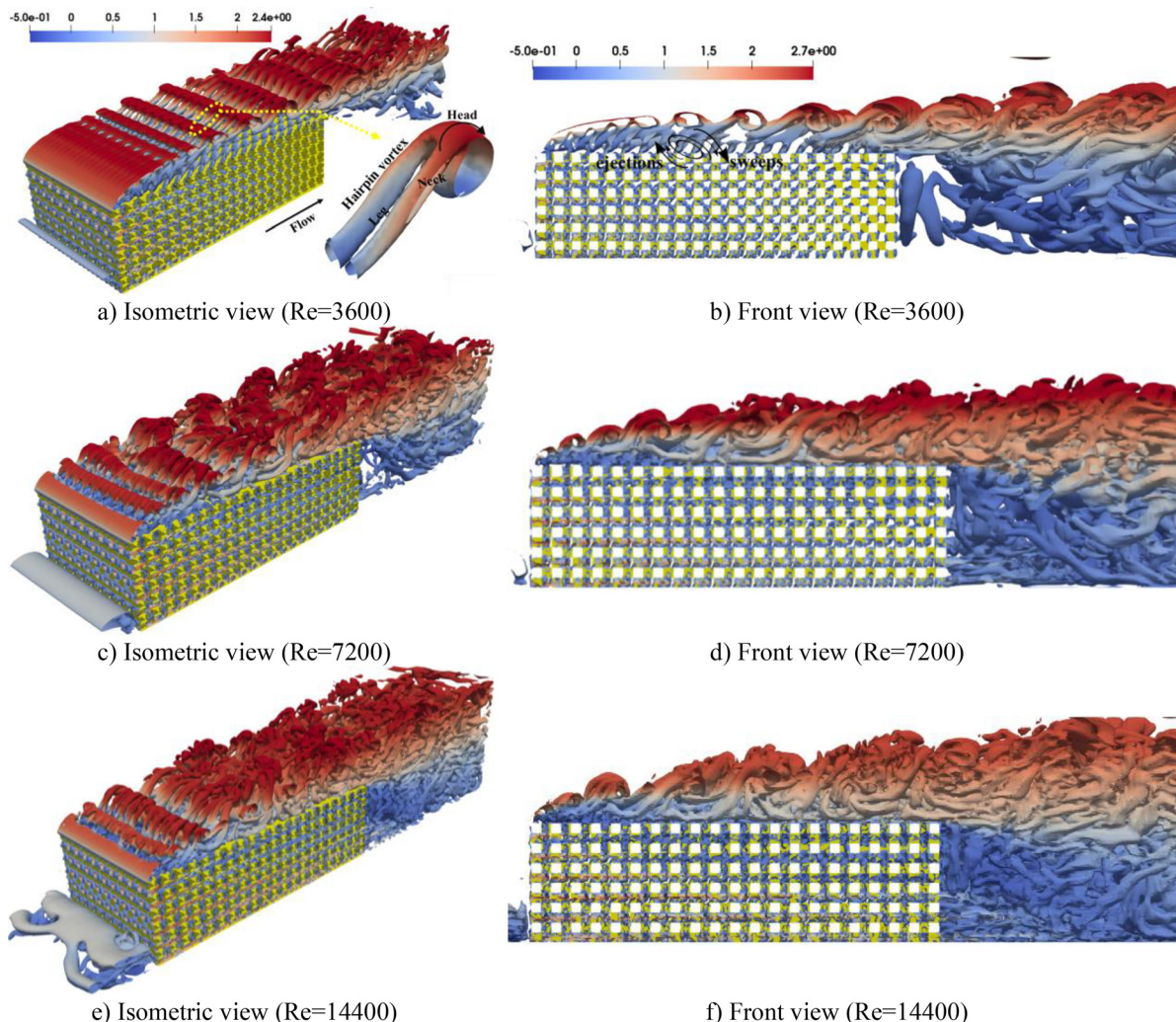


FIG. 10. Three-dimensional hairpin coherent structures identified by instantaneous iso-surface of $Q = 0.5 \times (\Omega^2 - S^2)$ criterion colored by instantaneous streamwise velocity; (a) and (b) isometric and front view of hairpin structures at $Re = 3600$, (c) and (d) isometric and front view of hairpin structures at $Re = 7200$, and (e) and (f) isometric and front view of hairpin structures at $Re = 14\,400$.

the leading edge of the porous block, the shear layer rolls up to form hairpin vortices and elongates downstream. In Figs. 10(a) and 10(b), for case 1 with $Re = 3600$, an organized series of hairpin vortices are recognized with spanwise-oriented heads, which are connected to hairpin legs. However, as the Re number increases ($Re = 7200$ and 14 400), the hairpin vortices deviate from the well-organized orientation [see Figs. 10(c)-10(f)]. It is worth noting that at $Re = 3600$, similar to the case of the impermeable wall,⁵³ the hairpin legs stretch longer and organized vortex motion is sustained by moving downstream. In contrast, the vortex motion cannot be preserved as the Re number enhances, resulting in shorter hairpin legs. The reason is that as the Re number increases, the legs of the hairpin vortices show more tendency to submerge into the permeable wall owing to the stronger sweep events near the interface, which are detailed quantitatively in the following quadrant-hole analysis sub-section, Fig. 11. On the contrary, the ejection events generated by the momentum flux from the porous

block to the non-porous region do not possess enough energy to preserve the longitudinal vortex motion and provide a balance with the submerged momentum flux (penetrated to porous block through sweep events) at larger Re numbers. This imbalance between the strength of energetic sweeps and less-energetic ejections at higher Re numbers leads to the shortening of hairpin legs, as reported in Suga *et al.*²⁰ and Manes *et al.*¹⁷ as well. Thus, as shown in Fig. 10, the hairpin legs become shorter as the Re raises.

1. Quadrant-hole analysis

The quadrant analysis is usually utilized to examine the momentum transfer within and above the porous interface. In quadrant analysis based on the signs of u' and v' , four quadrants can be extracted from events as follows: Q1 ($u' > 0$ and $v' > 0$), which are called outward intersection events; Q2 ($u' < 0$ and $v' > 0$) called as ejection

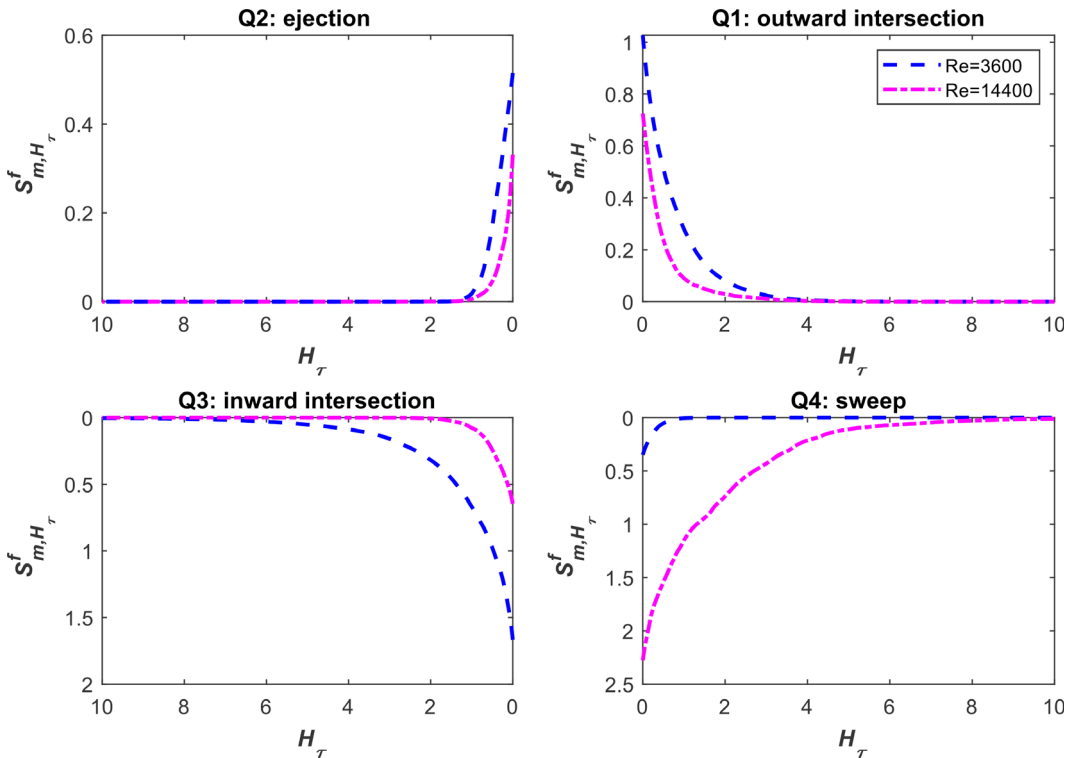


FIG. 11. Conditionally sampled of the Reynolds shear stress; comparison of the Reynolds stress fractions (S_{m,H_τ}^f) for different Re numbers at point ($X/D = 5$, $Y/D = 3.093$) at four quadrants.

events; $Q3 (u' < 0 \text{ and } v' < 0)$ called as inward intersection events; and $Q4 (u' > 0 \text{ and } v' < 0)$ called sweep events. According to Willmarth and Lu,⁵⁶ Raupach,⁵⁷ Zhai *et al.*,⁵⁸ and Suga *et al.*,²⁰ to evaluate the importance and contribution of different events at varying levels of strength, conditional sampling, called “quadrant hole analysis,” is performed based on the magnitude of a specific parameter in each quadrant. In quadrant analysis, the Reynolds stress fraction is estimated with the quadrant’s contribution to the total ensembled value as follows:

$$S_{m,H_\phi}^f = (\overline{u'v'})_{m,H_\phi} / (\overline{|u'v'|}) \times D_{m,H_\phi}^f, \quad (10)$$

where H_ϕ is denoted as the hole size corresponding to the variable ϕ for the conditional sampling. For instance, the hole size, based on the Reynolds shear stress, H_τ , is defined as

$$H_\tau = |(u'v')_{\text{threshold}}| / |\overline{u'v'}|. \quad (11)$$

In Eq. (10), $\overline{(\cdot)}$ denotes the ensemble averaging, while $\overline{(\cdot)}_m$ indicates averaging over the data in the quadrant m . $(\overline{u'v'})_{m,H_\phi}$ is the conditionally sampled of the Reynolds stress in quadrant m . This conditional sampling calculates the ensemble averaging of the Reynolds stress at time steps in which the magnitude of the shear stress in quadrant m surpasses the threshold. Thus, $(\overline{u'v'})_{m,H_\phi}$ can be calculated as

$$(\overline{u'v'})_{m,H_\phi} = \frac{1}{\sum N_m} \sum u'v'I_{m,H_\phi}, \quad (12)$$

where m is the indicator of four quadrants, 1 to 4, and N_m is the number of samples belonging to quadrant m . The indicator function I_{m,H_ϕ} satisfies the following condition:

$$I_{m,H_\phi} = \begin{cases} 1, & \text{if } (u', v') \text{ is in } Qm \text{ region and } |u'v'| > H_\phi |\overline{u'v'}|, \\ 0, & \text{otherwise.} \end{cases} \quad (13)$$

In Eq. (10), D_{m,H_ϕ}^f is the duration fraction in quadrant m and calculates the portion of the samples of Reynolds stress in which a certain level of a threshold, H_ϕ , is satisfied.

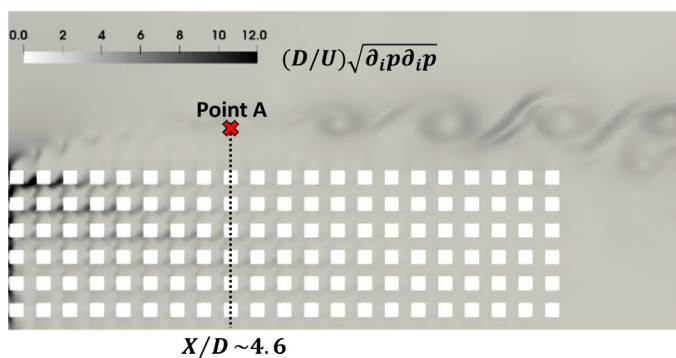
$$D_{m,H_\phi}^f = \frac{\sum I_{m,H_\phi}}{\sum N_m}. \quad (14)$$

The conditional sampling of the Reynolds shear stress (S_{m,H_τ}^f) of the Q1 to Q4 events against the hole size, H_τ , is depicted in Fig. 11 for Re numbers 3600 and 14 400. The results are presented for the coordinate ($X/D = 5$, $Y/D = 3.093$), and the style of presentation is compatible with the previous studies in the literature.^{20,57,58} It shows that as Re increases the S_{m,H_τ}^f reduces in Q2 events: the higher the Re number, the weaker the ejection events. In contrast, by increasing the Re number, the S_{m,H_τ}^f rises in Q4 events, as discussed in Fig. 10. This confirms the explanations in Fig. 10, meaning that at higher Re numbers, the sweep events become stronger, leading to shorter hairpin legs near the porous interface.

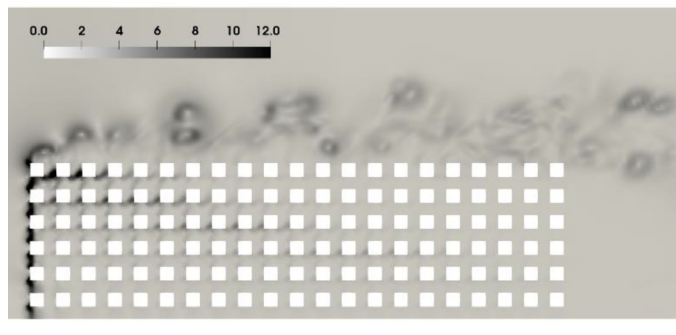
D. Kelvin-Helmholtz instability

Momentum exchange between the flow in porous and non-porous regions produces an inflectional shape of the mean velocity profile [see Fig. 12 (right)]. This inflection point coincides with the wall-normal location of $\partial^2 u / \partial y^2 = 0$ which typically occurs in the vicinity of the interface.⁵⁹ Pont-Vilchez *et al.*⁶⁰ discussed that around the inflection point, the well-known Kelvin-Helmholtz instabilities might be induced and elongated along the shear layer due to overtaking inertial forces to viscous forces. In addition, Suga *et al.*²⁰ asserted that the presence of hairpin vortices does not contradict the

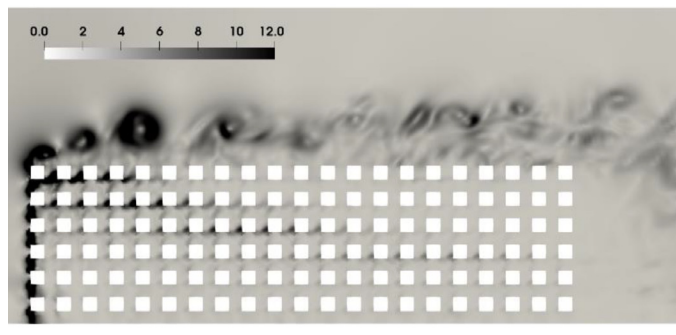
occurrence of K-H structures as they argue the latter could be superimposed on the formation and evolution mechanisms of hairpin vortex package and become more dominant as the Re number rises. Figure 12 displays K-H instabilities for three Re numbers, 3600, 7200, and 14 400, characterized by the magnitude of instantaneous pressure gradient normalized by the inlet velocity (U) and $D = 0.006$ m. The key reason that the current LES calculations include these three Re numbers is that the onset and evolution of K-H instabilities can be clearly captured and discussed in this range of Re numbers since it presents a wide range of different flow structures. Moreover, not only



a) Re=3600



b) Re=7200



c) Re=14400

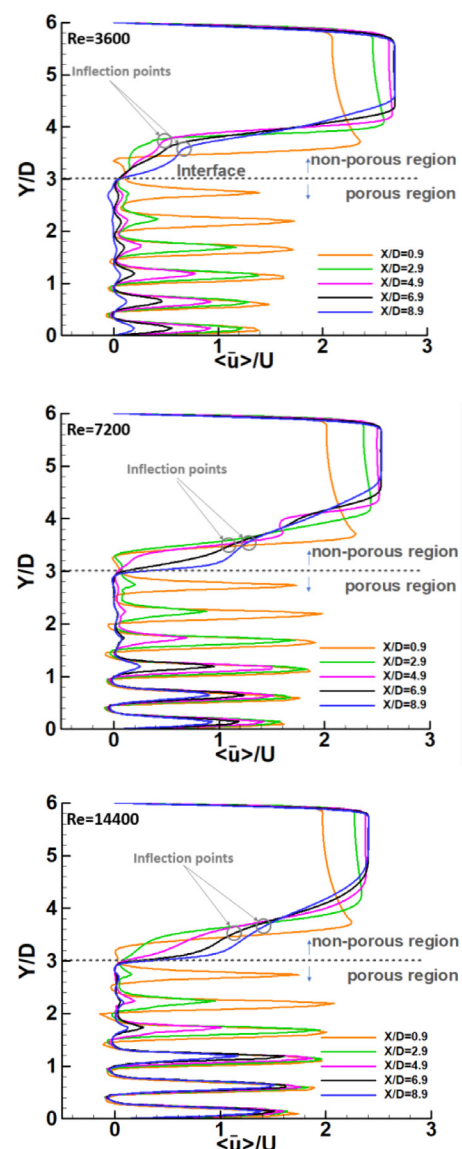
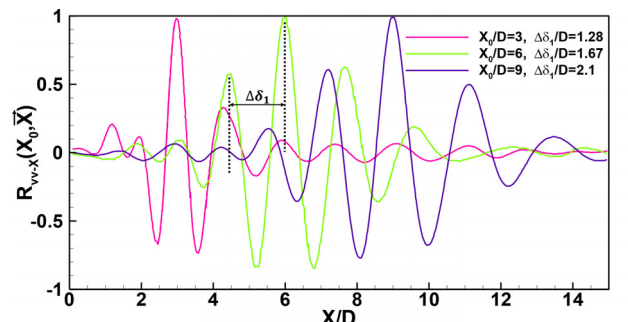


FIG. 12. Left: representation of Kelvin-Helmholtz instabilities identified by the non-dimensional magnitude of the instantaneous pressure gradient for different Re numbers, Right: vertical distribution of the non-dimensional time-averaged streamwise velocity ($\langle u \rangle / U$) at different locations, $X/D = 0.9, 2.9, 4.9, 6.9$, and 8.9 for three different Re numbers; (a) $Re = 3600$, (b) $Re = 7200$, and (c) $Re = 14\,400$.

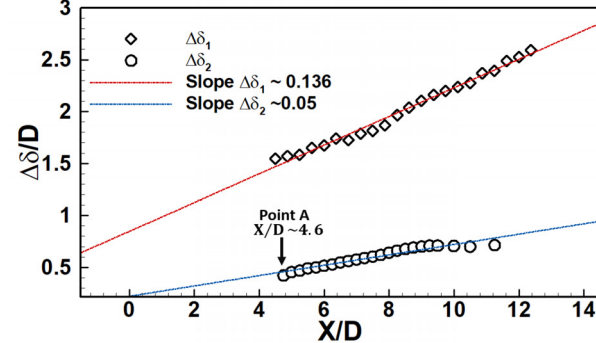
the current study but also the previous studies about the flow physics over and inside the porous block used this range of Re numbers in their work.^{20,21,25,61–63} At $Re = 3600$, the formation of K-H instabilities is retarded downstream, starting approximately at “Point A” with $\frac{X}{D} \sim 4.6$, as marked in Fig. 12(a). Before this point, the hairpin vortices (attached eddies) populate the shear layer and elongate downstream in an organized schematic, as can be observed in Figs. 10(a) and 10(b). This point (Point A) coincides with the sudden rise in TKE production, which will be discussed in detail in the TKE section [see Fig. 15(b)]. It is worth noting that before Point A the infinitesimal values of TKE production [Figs. 15(a) and 15(b)] demonstrates that there is no turbulence for $Re = 3600$ before $\frac{X}{D} \sim 4.6$. This means that the hairpin vortices’ formation before $X/D \sim 4.6$ occurs in a quasi-laminar boundary layer. This observation does not conflict with the findings of Manes *et al.*¹⁷ since the hairpin vortices can also be generated in the quasi-laminar boundary layer, as reported in Malkiel *et al.*⁶⁴ Here, the porous pores play a crucial role in triggering disturbances for forming hairpin vortices before $\frac{X}{D} \sim 4.6$ at $Re = 3600$. Figures 12(b) and 12(c) illustrate that for $Re = 7200$ and 14 400, the K-H instabilities embark just after the leading edge of the porous block. Thus, the shear layer is dominated by the K-H instabilities (shear instability eddies). It will be argued in Sec. III E that the commencement of the K-H instabilities coincides with the enhancement of Reynolds stress and, subsequently, TKE production.

1. The growth rate of K-H instabilities

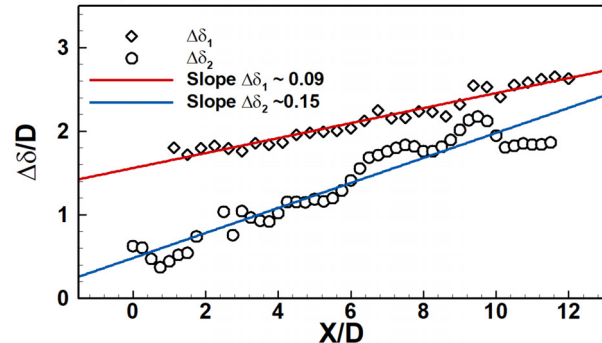
Here, the growth rate of K-H instabilities over the interface is examined in detail. Following Pont-Vilchez *et al.*⁶⁰ methodology, two parameters, $\Delta\delta_1$ and $\Delta\delta_2$, are defined to estimate the vortex size in streamwise and vertical directions generated by the K-H instability. $\Delta\delta_1$ represents the vortex size in the X -direction, which is calculated by two-point correlations of vertical velocity traversed in the streamwise direction [$R_{vv-X}(r_0, \vec{X})$]. For $\Delta\delta_1(r_0)$, the distance between two successive peaks in the $R_{vv-X}(r_0, \vec{X})$ is chosen as a metric to estimate the average vortex size in the X -direction and also the average distance between the vortices.⁶⁰ For instance, in Fig. 13(a), $\Delta\delta_1(r_0)$ is calculated for three reference points, $X/D = 3, 6$, and 9 , along the shear layer at $Re = 3600$. In addition, the vortex size in the vertical direction, named $\Delta\delta_2(X_0)$, is calculated by the two-point correlations of streamwise velocity traversed in the vertical direction [$R_{uu-Y}(r_0, \vec{Y})$]. For $\Delta\delta_2(r_0)$, the two times of the distance between the peak and zero values in the $R_{uu-Y}(r_0, \vec{Y})$ are employed as the relevant metric to estimate the vortex size in the vertical direction. Figures 13(b) and 13(c) display the streamwise distribution of $\Delta\delta_1$ and $\Delta\delta_2$. For $Re = 3600$, linear growth can be observed for both $\frac{\Delta\delta_1}{X} \sim 0.13$ and $\frac{\Delta\delta_2}{X} \sim 0.05$ along the shear layer in Fig. 13(b). At the beginning of the K-H instabilities, Point A with $X/D \sim 4.6$, the ratio of $\frac{\Delta\delta_1}{\Delta\delta_2} \sim 3.68$, which demonstrates an elliptic-like shape for the shear instability eddies that is consistent with the previous findings.⁶⁵ Of course, the elongation ratio, $\Delta\delta_1/\Delta\delta_2$, decreases gradually toward downstream up to $\frac{X}{D} \sim 8.75$ which implies that the elliptic-shape structures tend to reshape toward circular ones. For $Re = 14 400$ in Fig. 10(c), the K-H instabilities initiate just after the leading edge of the porous block. For this case, similar to $Re = 3600$, linear distributions for $\Delta\delta_1/X \sim 0.09$ and $\Delta\delta_2/X \sim 0.15$ are observed in Fig. 13(c). For $Re = 14 400$, by moving downstream, the elongation ratio, $\Delta\delta_1/\Delta\delta_2$, decreases significantly.



a) Two-point correlations of vertical velocity traversed in the streamwise direction, $R_{vv-X}(r_0, \vec{X})$, at $Re=3600$



b) $Re=3600$, along the streamwise direction at $Y/D=4$



c) $Re=14400$, along the streamwise direction at $Y/D=3.667$

FIG. 13. (a) Utilizing tow-point correlations for estimating $\Delta\delta_1$, (b) and (c) growth rate of K-H vortices ($\Delta\delta_1, \Delta\delta_2$) along the streamwise direction for $Re = 3600$ and $14 400$, respectively.

This implies that the elliptic-shape structures show more tendency to stretch along the vertical direction, resulting in circular-shape structures near the trailing edge of the porous block ($\Delta\delta_1 \sim \Delta\delta_2$ at $X/D = 10$).

2. K-H instabilities roll-up

In order to assess the effect of the Re number on the development of K-H instabilities’ roll-up and their corresponding elongation toward downstream, the probability density function (PDF) of vertical velocity fluctuations is examined in this section. Figure 14 describes the PDF of normalized vertical velocity fluctuations at various selected points for three Re numbers. According to Fig. 17 in Ref. 66, three

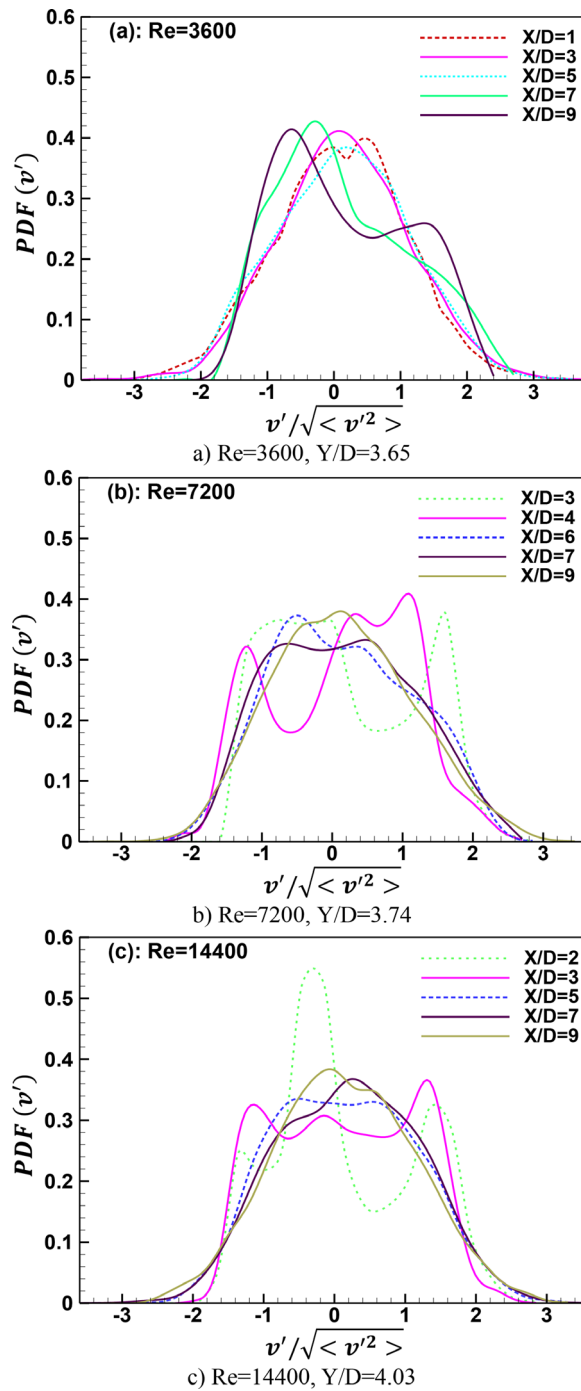


FIG. 14. PDFs of vertical velocity fluctuations at different locations for three cases: (a) $\text{Re} = 3600$, (b) $\text{Re} = 7200$, and (c) $\text{Re} = 14400$.

different patterns for K-H instability evolutions are introduced as follows: pattern 1) In the early stage, the rotational motion is restricted to a small fluid region around the low-speed vortex cores, resulting in well-organized rolling patterns [panel (1) in Fig. 17 of Ref. 66]. Since

the majority of the fluid in this panel is stagnant and convected downstream by the mean flow, its PDF resembles a Gaussian-like shape (single peaked shape) centered at zero with an infinitesimal standard deviation, as noted in Akula *et al.*,⁶⁶ pattern 2) At the intermediate stage, the K-H instabilities develop progressively and lead to the interaction of successive rolls, resulting in coherent structures [panel (2) in Fig. 17 of Ref. 66]. The relevant PDF of v' for this panel resembles a double-peaked shape. The PDF indicates that the majority of fluid possesses positive or negative velocities and a minority is stagnant;⁶⁶ pattern 3) When the rolls-up of K-H instability merges comprehensively, turbulent pockets emerge and an extensive range of velocity scales are observable [panel (3) in Fig. 17 of Ref. 66]. This phenomenon implies a flat shape for the PDF of v' .⁶⁶

For $\text{Re} = 3600$, the single-peaked shape of the PDF illustrates that most parts of the flow structures are similar to those in pattern 1 up to $X/D \sim 7$. At $X/D = 9$ (i.e., near the trailing edge), an additional peak emerges gradually, as shown in Fig. 14(a), emphasizing that the transition of turbulent structures from pattern 1 to 2 occurs in the vicinity of the trailing edge. In contrast, the PDFs of v' for $\text{Re} = 7200$ indicate that the turbulent K-H instability rolls-up resemble pattern 2 at the leading edge and preserves its shape up to $X/D = 4$. By moving further downstream, these rolls-up merge together and generate turbulent pockets (pattern 3), as seen in Fig. 14(b) at $X/D \sim 7$. Similar to $\text{Re} = 7200$, the K-H instability vortices produce pattern 2 for $\text{Re} = 14400$ at the leading edge (up to $X/D \sim 3$). However, this pattern transforms sooner to the turbulent pocket (pattern 3) compared to $\text{Re} = 7200$ by moving further downstream ($X/D \sim 5$). In other words, comparison of Figs. 14(b) and 14(c) demonstrates that the transition of turbulent structures from pattern 2 to 3 occurs earlier for $\text{Re} = 14400$.

E. Turbulent production and dissipation

Contours of turbulent kinetic energy, $TKE = 0.5(\langle u'^2 + v'^2 + w'^2 \rangle)$, and turbulence production, $P_k = -\langle u'_i u'_j \rangle \partial \langle \bar{u}_i \rangle / \partial X_j$, are depicted at trough planes for three Re numbers in Fig. 15. The TKE and turbulence production contours for $\text{Re} = 3600$ indicate that no turbulence exists at the leading edge up to approximately $X/D = 4.6$, denoted by Point A in Figs. 15(a) and 15(b). At nearly $X/D = 4.6$, around Point A, the turbulence production initiates, leading to the sudden growth of TKE, as observable in Fig. 15(a). The sudden rise of turbulence production at Point A for $\text{Re} = 3600$ coincides with the emergence of K-H instability vortices at this axial location, as described in Fig. 12(a). The K-H instability vortices then roll up along the shear layer and develop downstream. Their evolutionary pathways can be perceived in Figs. 15(a) and 15(b) by regions with higher values of TKE and turbulence production. At $\text{Re} = 7200$ and 14400, the sudden rise of turbulence production and, consequently, TKE occur just after the leading edge, as shown in Figs. 15(c)–15(f). This confirms the formation of K-H instabilities just at the leading edge for these two Re numbers [see Figs. 12(b) and 12(c)]. Compared to $\text{Re} = 7200$, a relatively higher level of turbulence can be observed inside the porous block for $\text{Re} = 14400$.

Figure 16 shows the instantaneous and time-averaged total dissipation ($\epsilon_t = -2\partial S'_{ij} S'_{ij} + \tau_{ij}^* S'_{ij}$, where $\tau_{ij}^* = \tau_{ij} - \tau_{kk} \delta_{ij}$) of turbulent kinetic energy at the trough plane for three Re numbers. As it can be seen, the overall distribution of instantaneous and time-averaged ϵ_t is similar to the TKE and K-H instability vortices in Figs. 15 and 12,

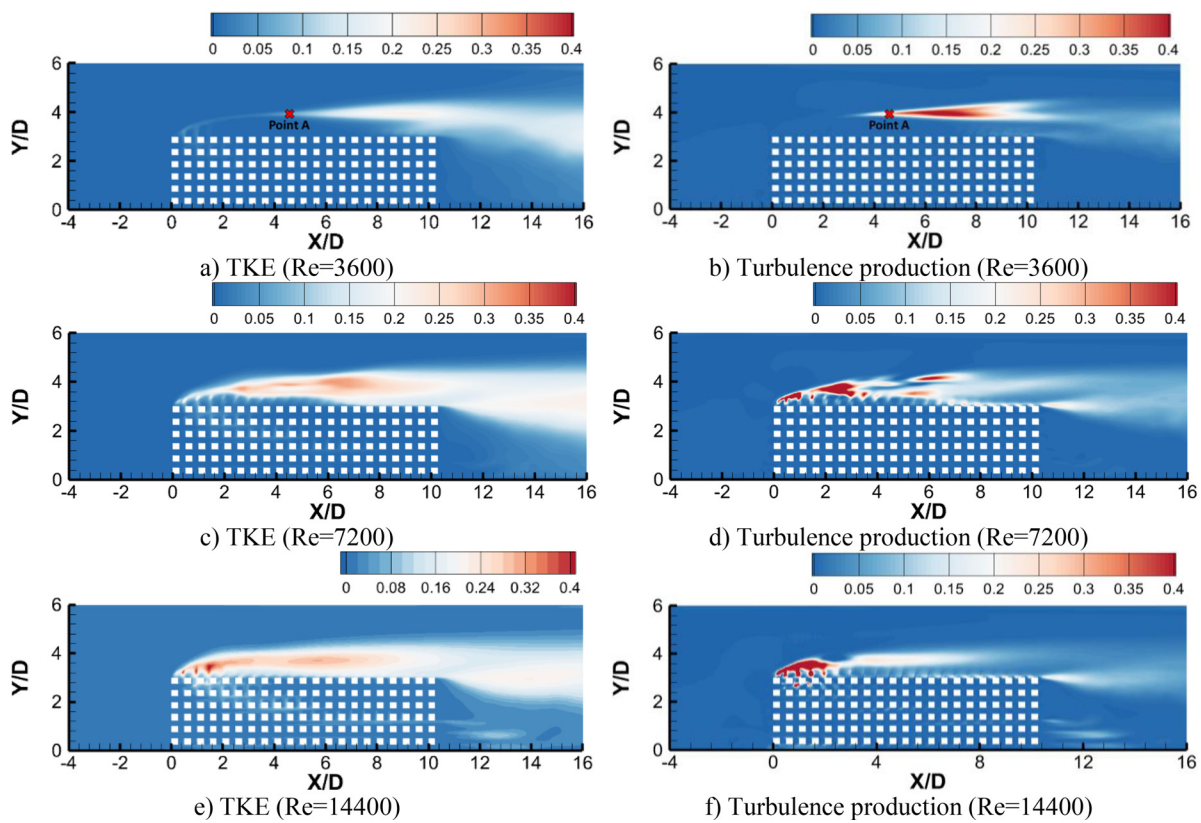


FIG. 15. Contours of turbulent kinetic energy (left) and turbulence production (right) for three cases at the trough plane; (a) and (b) TKE and turbulence production for $Re = 3600$, (c) and (d) TKE and turbulence production for $Re = 7200$, and (e) and (f) TKE and turbulence production for $Re = 14\,400$.

respectively. This indicates that over the porous–fluid interface, the total dissipation is influenced by the strong unstable shear layer. In other words, the higher magnitudes of the instantaneous and time-averaged total dissipation are the consequence of the strong unstable shear layer leading to the K–H instabilities. For $Re = 3600$ at nearly $X/D = 4.6$, around Point A, the dissipation of turbulence initiates and diffuses toward the downstream where higher values of TKE and turbulence production in Figs. 15(a) and 15(b) coincide with higher magnitudes of time-averaged ε_t . In addition, the distribution of instantaneous ε_t matches with the emergence of K–H instability vortices in Fig. 12(a). At higher Re number, the formation of K–H instabilities just at the leading edge [see Figs. 12(b) and 12(c)] matches with the different distribution of instantaneous and time-averaged total dissipation for $Re = 7200$ and $Re = 14\,400$, as can be seen in Figs. 16(c)–16(f); the sudden rise of turbulence production just after the leading edge [Figs. 15(d) and 15(f)] results in higher magnitudes of dissipation at this region.

F. Turbulence anisotropy

To investigate the anisotropic nature of the turbulent flow over the interface, the Reynolds stress anisotropy tensor (b_{ij}) defined as the difference between the Reynolds stress tensor components against TKE in the following equation is employed:

$$b_{ij} = \frac{\langle u'_i u'_j \rangle}{2k} - \frac{\delta_{ij}}{3}, \quad \text{where } k = \frac{\langle u'_m u'_m \rangle}{2}. \quad (15)$$

Eigenvalues of b_{ij} tensor ($\lambda_1, \lambda_2, \lambda_3$), attained from diagonalized b_{ij} , can be engaged to plot anisotropy invariant map (AIM), first introduced by Lumley and Newman.⁶⁷ The axes of AIMs are invariant properties of b_{ij} which are functions of eigenvalues λ_i , illustrating the componental traits of turbulence field, i.e., relative strengths of the different components of velocity fluctuations.⁶⁸ Some shortcomings of the Lumley triangle were removed by Choi and Lumley,⁶⁹ introducing the turbulence triangle as shown in Fig. 17. This triangle provides an accurate trajectory of the return to isotropy near the isotropic corner (X_{3c}).⁶⁸ The second $\eta = (\frac{1}{6} b_{ij} b_{ji})^{1/2}$ and third $\xi = (\frac{1}{6} b_{ij} b_{jn} b_{ni})^{1/3}$ invariants of b_{ij} represent two axes of the turbulence triangle in Fig. 17 and (σ_x, σ_y , and σ_z) are diagonal components of Reynolds stress tensor, i.e., $(u' u', v' v', w' w')$. As can be seen in Fig. 17, the axisymmetric turbulence is surrounded by left (axisymmetric contraction) and right (axisymmetric expansion) limits defined as $\eta = -\xi$ and $\eta = \xi$ lines, respectively. Whereas, the upper boundary of turbulence triangle, called two-component limit, is bounded by curve $\eta = \left(\frac{1}{27} + 2\xi^3\right)^{1/2}$. The left and right boundaries form the shape of oblate spheroid and prolate spheroid axisymmetric turbulence, which are called disk- and rod-like axisymmetric, correspondingly. The upper-curved limit

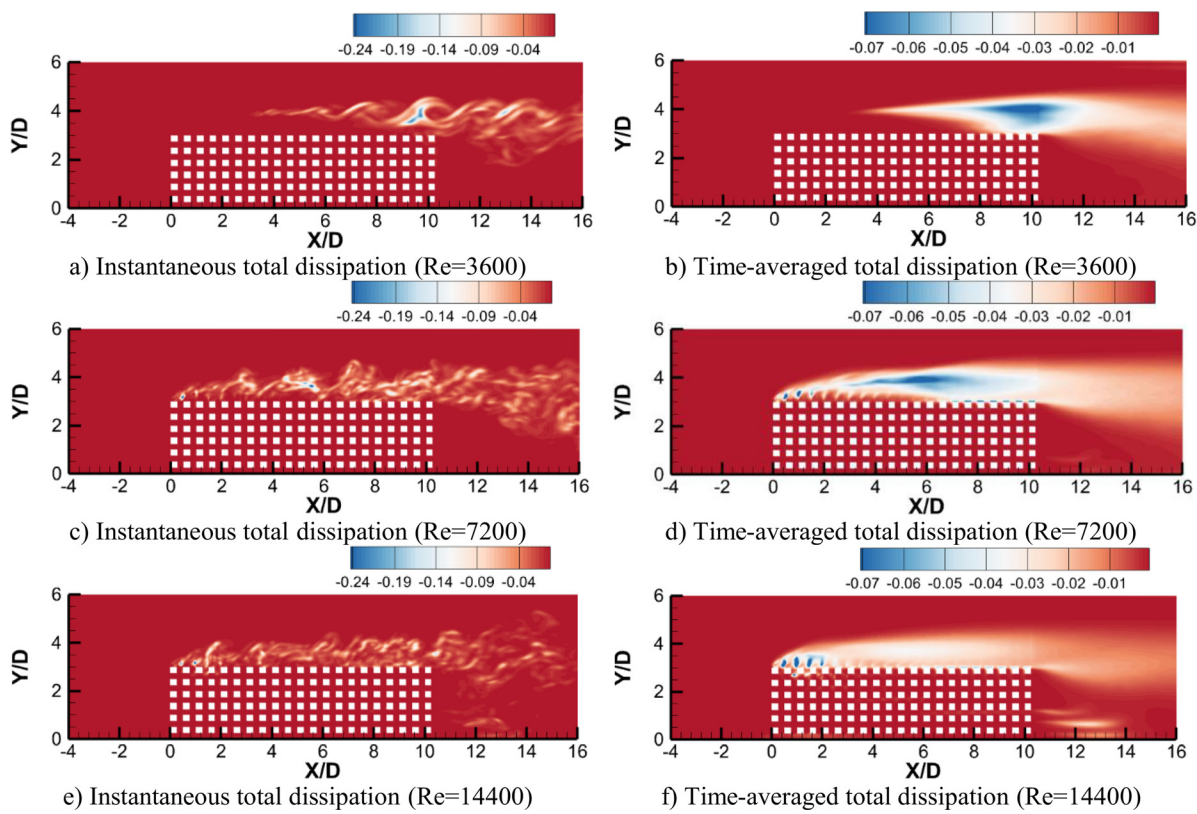


FIG. 16. Contours of instantaneous (left) and time-averaged total dissipation (right) for three Re numbers at the trough plane; (a) and (b) Instantaneous and time-averaged ϵ_t at $Re = 3600$, (c) and (d) Instantaneous and time-averaged ϵ_t at $Re = 7200$, (e) and (f) Instantaneous and time-averaged ϵ_t at $Re = 14\,400$.

possesses a two-component elliptical disk-like shape of turbulence. The boundaries in the turbulence triangle are connected by three particular states, X_{1c} , X_{2c} , and X_{3c} , denoting one component turbulence, two-components axisymmetric circular disk-like turbulence, and

three-component isotropic turbulence, respectively.^{70,71} A visualization technique introduced by Emory and Iaccarino⁶⁸ is employed to construct a color map superimposed on the turbulence triangle, as observable in Fig. 17. This provides information about the componentality of the turbulence field by assigning specific colors to different turbulence states. For this purpose, three common colors, red, green, and blue, are utilized to represent the one-component turbulence (X_{1c}), two-components turbulence (X_{2c}), and isotropic turbulence (X_{3c}), respectively. The other states of turbulence within the AIM are the combination of these three colors (red, green, and blue).⁶⁸

Figure 18 provides information about the turbulence anisotropy for three Re numbers by utilizing the turbulence triangle on horizontal lines crossing the center of K-H instability vortices. Figure 18(a) depicts the K-H instability vortices for $Re = 3600$, which are superimposed on the $u'u'$ contour. As can be seen in this figure, the wall-normal location of the marked points for the anisotropy analysis intersects with the center of the K-H instability vortices. The sudden rise of $u'u'$ at $X/D = 5$ (point P1) in Fig. 18(b), $Re = 3600$, and its proximity to X_{1c} in Fig. 18(c) indicate that, at this point, the turbulence is strongly one-component. This means that $u'u'$ dominates the other two components (vertical and spanwise Reynolds stresses) relatively. However, the other two components of Reynolds stresses, $v'v'$, $w'w'$, increase gradually by moving downstream from P1 to P4 for $Re = 3600$. This leads to strong variations along the axisymmetric expansion line toward isotropic turbulence ($u'u' \sim v'v' \sim w'w'$) in

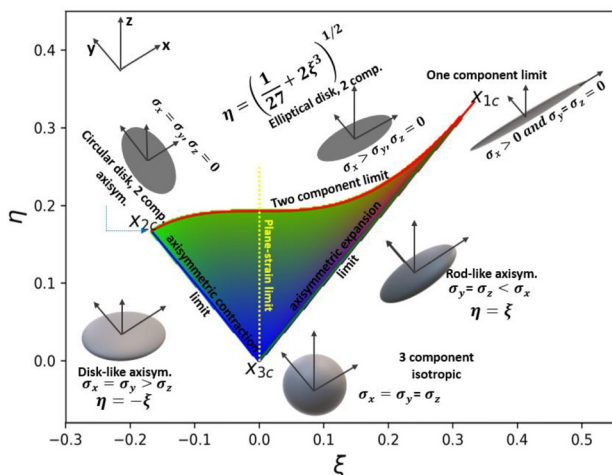


FIG. 17. Non-linear anisotropy invariant map (AIM), turbulence triangle, to characterize the turbulence states by invariant properties of Reynolds stress anisotropy tensor. Plane-strain limit shows the border of different components.^{68,71}

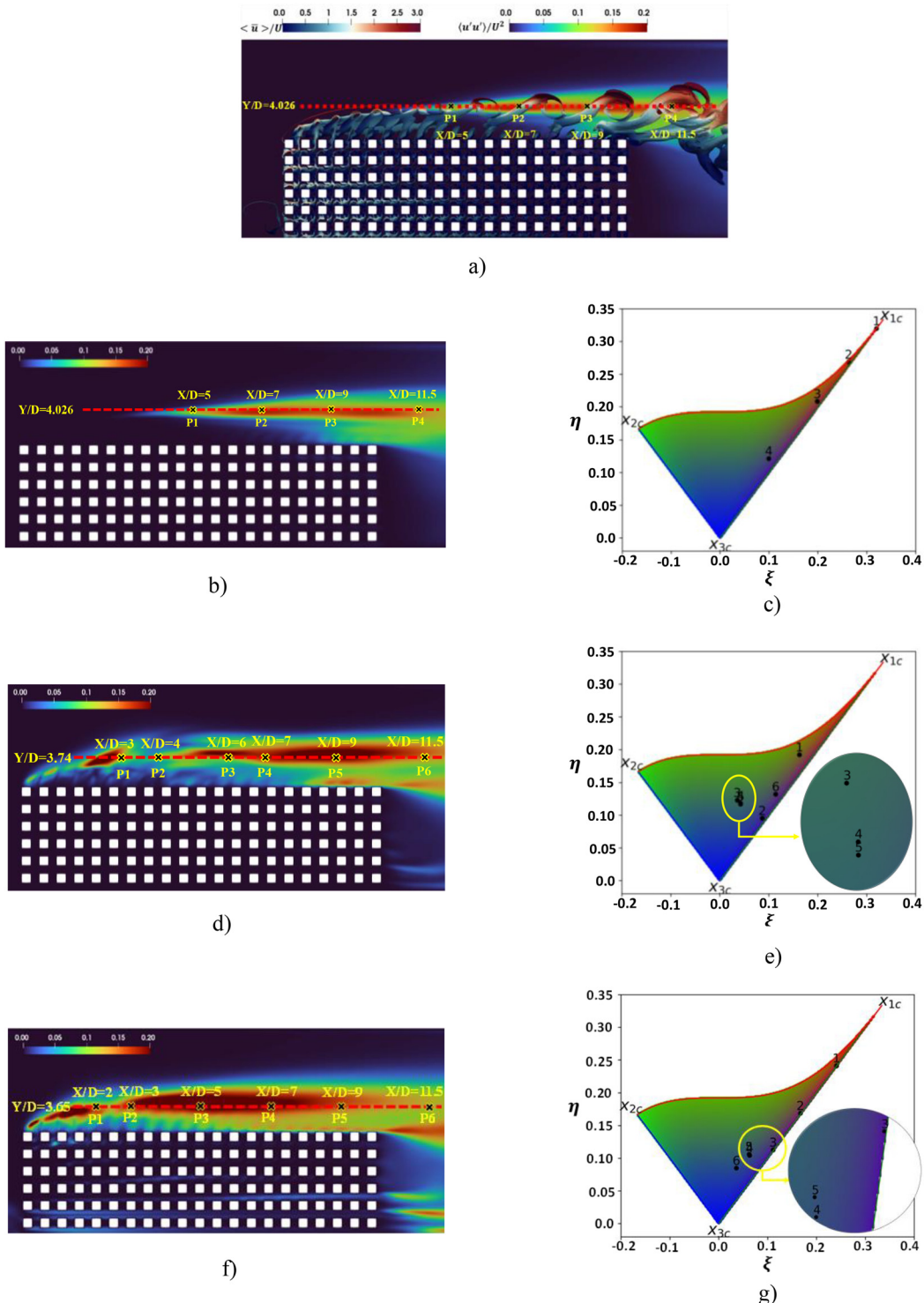


FIG. 18. (a) K–H instabilities identified by instantaneous iso-surface of Q-criterion colored by velocity magnitude are superimposed on streamwise Reynolds stress ($\langle u'u' \rangle / U^2$) contour at trough plane for $Re = 3600$, including marked locations along the streamwise direction to represent them in turbulence triangle, (b), (d), and (f) Streamwise Reynolds stress ($\langle u'u' \rangle / U^2$) contours at the trough plane for $Re = 3600, 7200$, and $14\,400$, respectively, including marked points traversed in X-direction to represent them in the turbulence triangle, and (c), (e), and (g) location of the marked points in the turbulence triangle.

corresponding turbulence triangle, Fig. 18(c). Of course, movement along the axisymmetric expansion limit emphasizes that the turbulence still preserves the rod-like shape with one larger eigenvalue due to the stronger $u'u'$ compared to the other components. The turbulence trajectory results for $Re = 7200$ and $14\,400$ are displayed in the turbulence triangles in Figs. 18(e) and 18(g) for points P1–P6. The overall variation of turbulence nature for $Re = 14\,400$ is similar to the $Re = 3600$. In comparison, some differences are detectable for $Re = 7200$. For $Re = 7200$, the turbulence at the starting point (P1) is a combination of rod-like axisymmetric and elliptical disk (two components). Moreover, the position of P1 in the turbulence triangle is far from X_{1c} owing to $u'u' > v'v' > w'w'$. Moving toward the trailing edge of the porous block yields in reshaping the turbulence nature to the isotropic state (X_{3c}) for $Re = 7200$. Of course, the coincidence of points P3 to P5 in the turbulence triangle for this case denotes that from $X/D = 6$ to 9, the state of the turbulence remains almost constant without any variations ($u'u' > v'v' > w'w'$). Further downstream at $X/D = 11.5$, the turbulence again reshapes toward rod-like axisymmetric with larger streamwise Reynolds stress than the other components. For $Re = 14\,400$, the turbulence trajectory initiates (P1, $X/D = 2$) from the vicinity of X_{1c} in the turbulence triangle ($u'u' \gg v'v' \sim w'w'$). Then, it reshapes toward the isotropic state (X_{3c}) by moving in the streamwise direction toward the trailing edge of the porous block. However, from P1 to P3 ($X/D = 2$ to 5), the variations are along the axisymmetric expansion line, indicating one larger eigenvalue rather than other ones. However, moving further downstream (from $\frac{X}{D} = 7$ to 11.5), the turbulence trajectory departs from the axisymmetric expansion line with the characteristics of $u'u' > v'v' > w'w'$. This means that the gradual increase of $v'v'$ overtakes that of $w'w'$.

IV. CONCLUSIONS

Pore-scale LES study is conducted for three Reynolds numbers in a composite porous fluid system. The primary objective of the present work is to explore the flow exchange between the porous and non-porous regions and its impact on Kelvin-Helmholtz (K-H) instabilities over the porous-fluid interface. To this end, quadrant-hole analysis, the growth rate of K-H instabilities, PDF of velocity fluctuations for analyzing K-H instability rolls-up, turbulence kinetic energy (TKE), turbulence production, and dissipation and turbulence anisotropy triangle are utilized in this study. The major findings of this paper are summarized as follows:

- (1) The flow leakage increases as the Re number decreases and prevents the formation of the mean turbulence separation bubble over the fluid-porous interface. Consequently, in the case of a lower Re, no reattachment point is observed in the mean streamlines of the flow over the interface. Moreover, for three Re numbers, more than 60% of the flow entering the porous blocks exit the porous interface within the first 75% of the porous block length; this becomes even more pronounced when the Re number decreases.
- (2) Flow visualization shows the counter-rotating vortex pair (CRVP) flow structures created inside the porous block and above the interface. The CRVPs develop in the deeper layers of the porous block and migrate upward in the vertical direction toward the interface. Larger CRVPs with stretched and farther centers from the interface are associated with the lower Re,

while smaller ones with contracted and closer centers to the interface are associated with the higher Re.

- (3) As a result of the collision between the main flow and the low-speed flow lump, the shear layer rolls up at the leading edge of the porous block, causing the formation of hairpin structures. $Re = 3600$ shows a series of well-organized hairpin vortices with spanwise-oriented heads connected to longer hairpin legs. In contrast, by raising the Re number, the hairpin vortices depart from the well-organized pattern with shorter legs. The quadrant-hole analysis demonstrated that raising the Re number makes the sweep events stronger and submerges the hairpin vortices to the permeable walls. The imbalance between energetic sweeps and less-energetic ejections at higher Re numbers makes the hairpin legs shorter.
- (4) The turbulence production is significantly different for the three Re numbers. For $Re = 3600$, the turbulence production retarded downstream, while for $Re = 7200$ and $14\,400$, it initiates just after the leading edge of the porous block. In addition, the visualization of the K-H instabilities confirmed that K-H instability vortices coincide with the enhancement of turbulence production. Therefore, at $Re = 3600$, the formation of the K-H instabilities is delayed downstream, while those for $Re = 7200$ and $14\,400$ emerge just after the leading edge of the porous block.
- (5) There is a linear growth rate for the K-H instability vortices in the vertical and streamwise directions for $Re = 3600$ and $14\,400$. In both cases, the elliptic shape of the K-H instability vortices, detected at the beginning of the porous block, tends to reshape toward a circular shape (elongation ratio ~ 1) as they proceed downstream. For $Re = 14\,400$, the variation of elongation ratio is higher than for $Re = 3600$.
- (6) Using the probability density function (PDF) of velocity fluctuations, the effect of the Re number on the development and elongation of K-H instabilities' rolls-up is investigated. Different evolutionary patterns of K-H rolls-up for three Re numbers are observed based on the multiple peaks in the distribution of PDFs. In contrast to the higher Re numbers, the transition of the K-H rolls-up into the "turbulent packet" pattern is postponed to the trailing edge for $Re = 3600$.
- (7) The turbulence anisotropy analysis using the turbulence triangle showed that near the beginning of the K-H instabilities, the turbulence state is almost one-component for $Re = 3600$. By moving downstream, substantial variations are observed along the axisymmetric expansion line toward isotropic turbulence. As for $Re = 14\,400$, similar turbulence trajectories are noted, starting from nearly one-component turbulence at the leading edge and reshaping into isotropic turbulence as it moves toward the trailing edge. Near the leading edge, the turbulence nature differs for $Re = 7200$, as it is composed of both rod-like axisymmetric and two-components elliptical shape, though at the trailing edge, it reshaped into the isotropic one.

ACKNOWLEDGMENTS

This work was supported by the UK Engineering and Physical Sciences Research Council (EPSRC) (Grant Nos. EP/T012242/1 and EP/T012242/2). The authors would like to acknowledge the

assistance given by Research IT and the use of the Computational Shared Facility at The University of Manchester.

AUTHOR DECLARATIONS

Conflict of Interest

The authors have no conflicts to disclose.

Author Contributions

Mohammad Jadidi: Conceptualization (equal), Data curation (lead), Formal analysis (lead), Investigation (equal), Methodology (lead), Project administration (equal), Software (lead), Supervision (supporting), Validation (lead), Visualization (lead), Writing – original draft (lead), and Writing – review & editing (equal). **Hanieh Khalili Param:** Conceptualization (supporting), Formal analysis (supporting), Investigation (supporting), Methodology (supporting), Visualization (supporting), Writing – original draft (equal), and Writing – review & editing (equal). **Alistair James Revell:** Conceptualization (supporting), Formal analysis (supporting), Investigation (supporting), Methodology (supporting), Supervision (supporting), Validation (supporting), Writing – original draft (supporting), and Writing – review & editing (supporting). **Yasser Mahmoudi:** Conceptualization (equal), Formal analysis (supporting), Funding acquisition (lead), Investigation (supporting), Methodology (supporting), Project administration (equal), Resources (equal), Software (supporting), Supervision (lead), Validation (supporting), Visualization (supporting), Writing – original draft (supporting), and Writing – review & editing (equal).

DATA AVAILABILITY

The data that support the findings of this study are available from the corresponding author upon reasonable request.

REFERENCES

- ¹G. K. Marri and C. Balaji, “Experimental and numerical investigations on the effect of porosity and PPI gradients of metal foams on the thermal performance of a composite phase change material heat sink,” *Int. J. Heat Mass Transfer* **164**, 120454 (2021).
- ²R. Singh, A. Akbarzadeh, and M. Mochizuki, “Sintered porous heat sink for cooling of high-powered microprocessors for server applications,” *Int. J. Heat Mass Transfer* **52**(9–10), 2289–2299 (2009).
- ³Y. Mahmoudi, K. Hooman, and K. Vafai, *Convective Heat Transfer in Porous Media*, 1st ed. (CRC Press, Boca Raton, 2019).
- ⁴Y. Wang, Y. Yu, Z. Jing, C. Wang, G. Zhou, and W. Zhao, “Thermal performance of lithium-ion batteries applying forced air cooling with an improved aluminium foam heat sink design,” *Int. J. Heat Mass Transfer* **167**, 120827 (2021).
- ⁵C. Zhao *et al.*, “Simulations of melting performance enhancement for a PCM embedded in metal periodic structures,” *Int. J. Heat Mass Transfer* **168**, 120853 (2021).
- ⁶R. Attarzadeh, M. Rovira, and C. Duwig, “Design analysis of the ‘Schwartz D’ based heat exchanger: A numerical study,” *Int. J. Heat Mass Transfer* **177**, 121415 (2021).
- ⁷Z.-Z. Li, Y.-D. Ding, Q. Liao, M. Cheng, and X. Zhu, “An approach based on the porous media model for numerical simulation of 3D finned-tubes heat exchanger,” *Int. J. Heat Mass Transfer* **173**, 121226 (2021).
- ⁸S. A. S. Ali, M. Azarpayvand, and C. R. I. Da Silva, “Trailing-edge flow and noise control using porous treatments,” *J. Fluid Mech.* **850**, 83–119 (2018).
- ⁹C. Teruna, F. Avallone, D. Ragni, and D. Casalino, “On the noise reduction of a porous trailing edge applied to an airfoil at lifting condition,” *Phys. Fluids* **33**(5), 055132 (2021).
- ¹⁰R. Buccolieri *et al.*, “Analysis of local scale tree–atmosphere interaction on pollutant concentration in idealized street canyons and application to a real urban junction,” *Atmos. Environ.* **45**(9), 1702–1713 (2011).
- ¹¹A. M. Endalew *et al.*, “CFD modelling and wind tunnel validation of airflow through plant canopies using 3D canopy architecture,” *Int. J. Heat Fluid Flow* **30**(2), 356–368 (2009).
- ¹²S. Tschigale, B. Löhrer, R. Meller, and J. Fröhlich, “Large eddy simulation of the fluid–structure interaction in an abstracted aquatic canopy consisting of flexible blades,” *J. Fluid Mech.* **916**, A43 (2021).
- ¹³A. F. Zagni and K. V. Smith, “Channel flow over permeable beds of graded spheres,” *J. Hydraul. Div.* **102**(2), 207–222 (1976).
- ¹⁴F. Kong and J. Schetz, “Turbulent boundary layer over porous surfaces with different surfacegeometries,” in *20th Aerospace Sciences Meeting* (American Institute of Aeronautics and Astronautics, 1982).
- ¹⁵G. S. Beavers and D. D. Joseph, “Boundary conditions at a naturally permeable wall,” *J. Fluid Mech.* **30**(1), 197–207 (1967).
- ¹⁶H. J. Zippe and W. H. Graf, “Turbulent boundary-layer flow over permeable and non-permeable rough surfaces,” *J. Hydraul. Res.* **21**(1), 51–65 (1983).
- ¹⁷C. Manes, D. Poggi, and L. Ridolfi, “Turbulent boundary layers over permeable walls: Scaling and near-wall structure,” *J. Fluid Mech.* **687**, 141–170 (2011).
- ¹⁸T. Kim, G. Blois, J. L. Best, and K. T. Christensen, “Experimental study of turbulent flow over and within cubically packed walls of spheres: Effects of topography, permeability and wall thickness,” *Int. J. Heat Fluid Flow* **73**, 16–29 (2018).
- ¹⁹G. Rousseau and C. Ancey, “Scanning PIV of turbulent flows over and through rough porous beds using refractive index matching,” *Exp. Fluids* **61**(8), 172 (2020).
- ²⁰K. Suga, M. Mori, and M. Kaneda, “Vortex structure of turbulence over permeable walls,” *Int. J. Heat Fluid Flow* **32**(3), 586–595 (2011).
- ²¹K. Suga, Y. Matsumura, Y. Ashitaka, S. Tominaga, and M. Kaneda, “Effects of wall permeability on turbulence,” *Int. J. Heat Fluid Flow* **31**(6), 974–984 (2010).
- ²²C. Manes, D. Pokrajac, I. McEwan, and V. Nikora, “Turbulence structure of open channel flows over permeable and impermeable beds: A comparative study,” *Phys. Fluids* **21**(12), 125109 (2009).
- ²³W. Breugem, B. Boersma, and R. Uittenbogaard, “The influence of wall permeability on turbulent channel flow,” *J. Fluid Mech.* **562**, 35–72 (2006).
- ²⁴M. Ghosh and R. Das, “Influence of form-induced shear stress on turbulent kinetic energy budget distributions above and within the flow–gravel-bed interface in permeable gravel bed stream—A comparative study,” *Water Resour.* **48**(4), 544–556 (2021).
- ²⁵X. Chu, W. Wang, G. Yang, A. Terzis, R. Helming, and B. Weigand, “Transport of turbulence across permeable interface in a turbulent channel flow: Interface-resolved direct numerical simulation,” *Transp. Porous Media* **136**(1), 165–189 (2021).
- ²⁶K. Suga and Y. Kuwata, “Turbulence over/inside porous surfaces and challenges to its modelling,” *J. Phys.: Conf. Ser.* **530**(1), 012004 (2014).
- ²⁷S. B. Naqvi and A. Bottaro, “Interfacial conditions between a free-fluid region and a porous medium,” *Int. J. Multiphase Flow* **141**, 103585 (2021).
- ²⁸H. Nepf and M. Ghisalberti, “Flow and transport in channels with submerged vegetation,” *Acta Geophys.* **56**(3), 753–777 (2008).
- ²⁹Y. Kuwata and K. Suga, “Extensive investigation of the influence of wall permeability on turbulence,” *Int. J. Heat Fluid Flow* **80**, 108465 (2019).
- ³⁰K. Suga, Y. Okazaki, and Y. Kuwata, “Characteristics of turbulent square duct flows over porous media,” *J. Fluid Mech.* **884**, A7 (2020).
- ³¹F. S. Anuar, I. A. Abdi, and K. Hooman, “Flow visualization study of partially filled channel with aluminium foam block,” *Int. J. Heat Mass Transfer* **127**, 1197–1211 (2018).
- ³²F. S. Anuar, K. Hooman, M. R. Malayeri, and I. A. Abdi, “Experimental study of particulate fouling in partially filled channel with open-cell metal foam,” *Exp. Therm. Fluid Sci.* **110**, 109941 (2020).
- ³³M. Jadidi, A. Revell, and Y. Mahmoudi, “Pore-scale large eddy simulation of turbulent flow and heat transfer over porous media,” *Appl. Therm. Eng.* **215**, 118916 (2022).
- ³⁴J. Voermans, M. Ghisalberti, and G. Ivey, “The variation of flow and turbulence across the sediment–water interface,” *J. Fluid Mech.* **824**, 413–437 (2017).
- ³⁵S. B. Pope, *Turbulent Flows* (Cambridge University Press, 2000).

- ³⁶P. Sagaut, *Large Eddy Simulation for Incompressible Flows: An Introduction* (Springer Science & Business Media, 2006).
- ³⁷W.-W. Kim, S. Menon, W.-W. Kim, and S. Menon, “Application of the localized dynamic subgrid-scale model to turbulent wall-bounded flows,” in *35th Aerospace Sciences Meeting and Exhibit*, Technical Report (AIAA, 1997), p. 210.
- ³⁸TO Foundation, see <https://cfd.direct/openfoam/user-guide/> for “OpenFOAM v9 User Guide.”
- ³⁹I. B. Celik, Z. N. Cehreli, and I. Yavuz, “Index of resolution quality for large eddy simulations,” *J. Fluids Eng.* **127**(5), 949–958 (2005).
- ⁴⁰I. Celik, M. Klein, and J. Janicka, “Assessment measures for engineering LES applications,” *J. Fluids Eng.* **131**(3), 031102 (2009).
- ⁴¹S. B. Pope, “Ten questions concerning the large-eddy simulation of turbulent flows,” *New J. Phys.* **6**(1), 35 (2004).
- ⁴²L. Davidson, “Large eddy simulations: How to evaluate resolution,” *Int. J. Heat Fluid Flow* **30**(5), 1016–1025 (2009).
- ⁴³L. Davidson, “How to estimate the resolution of an LES of recirculating flow,” in *Quality and Reliability of Large-Eddy Simulations II* (Springer Netherlands, 2011), pp. 269–286.
- ⁴⁴H. Wurps, G. Steinfeld, and S. Heinz, “Grid-resolution requirements for large-eddy simulations of the atmospheric boundary layer,” *Boundary-Layer Meteorol.* **175**(2), 179–201 (2020).
- ⁴⁵F. Bazdidi-Tehrani, A. Ghafouri, and M. Jadidi, “Grid resolution assessment in large eddy simulation of dispersion around an isolated cubic building,” *J. Wind Eng. Ind. Aerodyn.* **121**, 1–15 (2013).
- ⁴⁶J. Pelmard, S. Norris, and H. Friedrich, “LES grid resolution requirements for the modelling of gravity currents,” *Computers & Fluids* **174**(5), 256–270 (2018).
- ⁴⁷J.-M. Leu, H.-C. Chan, and M. Chu, “Comparison of turbulent flow over solid and porous structures mounted on the bottom of a rectangular channel,” *Flow Meas. Instrum.* **19**(6), 331–337 (2008).
- ⁴⁸R. Poletto, T. Craft, and A. Revell, “A new divergence free synthetic eddy method for the reproduction of inlet flow conditions for LES,” *Flow, Turbul. Combust.* **91**(3), 519–539 (2013).
- ⁴⁹S. Ergun, “Fluid flow through packed columns,” *J. Chem. Eng. Prog.* **48**(2), 89–94 (1952).
- ⁵⁰M. Nazari, D. Jalali Vahid, R. K. Saray, and Y. Mahmoudi, “Experimental investigation of heat transfer and second law analysis in a pebble bed channel with internal heat generation,” *Int. J. Heat Mass Transfer* **114**, 688–702 (2017).
- ⁵¹J. S. Lee and K. Ogawa, “Pressure drop though packed bed,” *J. Chem. Eng. Jpn.* **27**(5), 691–693 (1994).
- ⁵²T. Theodorsen, “The structure of turbulence,” in *50 Jahre Grenzschichtforschung: Eine Festschrift in Originalbeiträgen*, edited by H. Görtler and W. Tollmien (Vieweg+Teubner Verlag, Wiesbaden, 1955), pp. 55–62.
- ⁵³R. J. Adrian, C. D. Meinhart, and C. D. Tomkins, “Vortex organization in the outer region of the turbulent boundary layer,” *J. Fluid Mech.* **422**, 1–54 (2000).
- ⁵⁴R. Volino, M. Schultz, and K. Flack, “Turbulence structure in rough-and-smooth-wall boundary layers,” *J. Fluid Mech.* **592**, 263–293 (2007).
- ⁵⁵Y. Wu and K. T. Christensen, “Spatial structure of a turbulent boundary layer with irregular surface roughness,” *J. Fluid Mech.* **655**, 380–418 (2010).
- ⁵⁶W. Willmarth and S. Lu, “Structure of the Reynolds stress near the wall,” *J. Fluid Mech.* **55**(1), 65–92 (1972).
- ⁵⁷M. Raupach, “Conditional statistics of Reynolds stress in rough-wall and smooth-wall turbulent boundary layers,” *J. Fluid Mech.* **108**, 363–382 (1981).
- ⁵⁸W. Zhu, R. Van Hout, and J. Katz, “PIV measurements in the atmospheric boundary layer within and above a mature corn canopy. Part II: Quadrant-hole analysis,” *J. Atmos. Sci.* **64**(8), 2825–2838 (2007).
- ⁵⁹P. G. Drazin and W. H. Reid, *Hydrodynamic Stability*, 2nd ed. (Cambridge University Press, 2004).
- ⁶⁰A. Pont-Vilchez, F. Trias, A. Gorobets, and A. Oliva, “Direct numerical simulation of backward-facing step flow at and expansion ratio 2,” *J. Fluid Mech.* **863**, 341–363 (2019).
- ⁶¹Y. Kuwata and K. Suga, “Transport mechanism of interface turbulence over porous and rough walls,” *Flow, Turbul. Combust.* **97**(4), 1071–1093 (2016).
- ⁶²Y. Kuwata and K. Suga, “Direct numerical simulation of turbulence over anisotropic porous media,” *J. Fluid Mech.* **831**, 41–71 (2017).
- ⁶³Q. Al-Aabid, T. J. Craft, and H. Iacovides, “Improved eddy-viscosity modelling of turbulent flow around porous-fluid interface regions,” *Transp. Porous Media* **131**(2), 569–594 (2020).
- ⁶⁴E. Malkiel, V. Levinski, and J. Cohen, “The evolution of a localized vortex disturbance in external shear flows. Part 2. Comparison with experiments in rotating shear flows,” *J. Fluid Mech.* **379**, 351–380 (1999).
- ⁶⁵C. D. Winant and F. K. Browand, “Vortex pairing: The mechanism of turbulent mixing-layer growth at moderate Reynolds number,” *J. Fluid Mech.* **63**(2), 237–255 (1974).
- ⁶⁶B. Akula, P. Suchandra, M. Mikhaeil, and D. Ranjan, “Dynamics of unstably stratified free shear flows: An experimental investigation of coupled Kelvin-Helmholtz and Rayleigh-Taylor instability,” *J. Fluid Mech.* **816**, 619–660 (2017).
- ⁶⁷J. L. Lumley and G. R. Newman, “The return to isotropy of homogeneous turbulence,” *J. Fluid Mech.* **82**(1), 161–178 (1977).
- ⁶⁸M. Emory and G. Iaccarino, “Visualizing turbulence anisotropy in the spatial domain with componentality contours,” in *Center for Turbulence Research Annual Research Briefs* (Center for Turbulence Research, 2014), pp. 123–138.
- ⁶⁹K.-S. Choi and J. L. Lumley, “The return to isotropy of homogeneous turbulence,” *J. Fluid Mech.* **436**, 59–84 (2001).
- ⁷⁰S. Dey, G. Ravi Kishore, O. Castro-Orgaz, and S. Z. Ali, “Turbulent length scales and anisotropy in submerged turbulent plane offset jets,” *J. Hydraul. Eng.* **145**(2), 04018085 (2019).
- ⁷¹M. Andersson, T. Ebbers, and M. Karlsson, “Characterization and estimation of turbulence-related wall shear stress in patient-specific pulsatile blood flow,” *J. Biomech.* **85**, 108–117 (2019).